Chair for Dark Matter - E47
TUM School of Natural Sciences
Technische Universität München

Commissioning and Characterisation of a low-background Silicon Drift Detector Setup at the Canfranc Deep Underground Laboratory

Thesis for the degree of Master of Science
at the TUM School of Natural Sciences
Technische Universität München

Supervisors:	Prof. Dr. rer. nat. Susanne Mertens Dr. Christoph Wiesinger Dr. Frank Edzards
Second Corrector:	Dr. Raimund Strauß
Submitted by:	Joanna Bilicki, B.Sc.
Submitted on:	November 27th, 2023

Master Thesis
27th of November 2023

Abstract

The International AXion Observatory (IAXO) will be looking for solar axions. Using a strong magnetic field the axion particles are converted to X-rays via the Primakoff effect. The sensitivity of this rare-event search will strongly depend on the background performance of the X-ray detection system. In addition, the X-ray detector needs to have a high efficiency, good energy resolution and low energy threshold. BabyIAXO is a scaled down version of IAXO and it will test all components of the final experiment as well as explore new axion parameter space. The upper limit of the required background index for BabyIAXO is 10^{-7} cts/keV/s/cm^2. A possible detector candidate is the TRISTAN silicon drift detector (SDD). It features a good energy resolution of less than 200 eV at 5.9 keV for photons at room temperature, a low energy threshold of 1 keV and a high detection efficiency of more than 95 % in the region of interest between 1 keV to 10 keV. Solely the ability of the TRISTAN SDD to reach the required ultra-low background level has yet to be confirmed.

In this thesis the background measurement of a seven pixel TRISTAN SDD in a dedicated shielding setup is described. It was performed in a dedicated experimental setup in the deep underground laboratory in Canfranc (LSC) acquiring data of 116 days. The measurement was stable with a maximal drift in energy of 1.5 %. The determined resolution lies between 240 eV to 384 eV at 6 keV due to sub-optimal noise conditions. With this measurement a background index of $(5.9 \pm 0.5) \times 10^{-6}$ counts/keV/s/cm^2 was obtained. This background level still exceeds the requirements of BabyIAXO. The spectral information indicated radio-impurities in the close-by vicinity of the SDD and is consistent with a simulation as well as the low radiopurity of the printed circuit board (PCB), which was shown by a screening measurement after the background measurement had been started. An upcoming upgrade of the detector will therefore feature PCB material with improved radiopurity.

Declaration of Authorship

I hereby declare that the thesis submitted is my own unaided work. All direct or indirect sources used are acknowledged as references. I am aware that the thesis in digital form can be examined for the use of unauthorized aid and in order to determine whether the thesis as a whole or parts incorporated in it may be deemed as plagiarism. For the comparison of my work with existing sources I agree that it shall be entered in a database where it shall also remain after examination, to enable comparison with future theses submitted. Further rights of reproduction and usage, however, are not granted here. This thesis was not previously presented to another examination board and has not been published[1].

München, November 27th, 2023

Contents

1 Axions

When looking at the content of the universe three components can be identified. The ordinary matter makes up the smallest part, followed by dark matter and then dark energy. Figure 1.1 displays the composition measured by the Planck satellite [3].

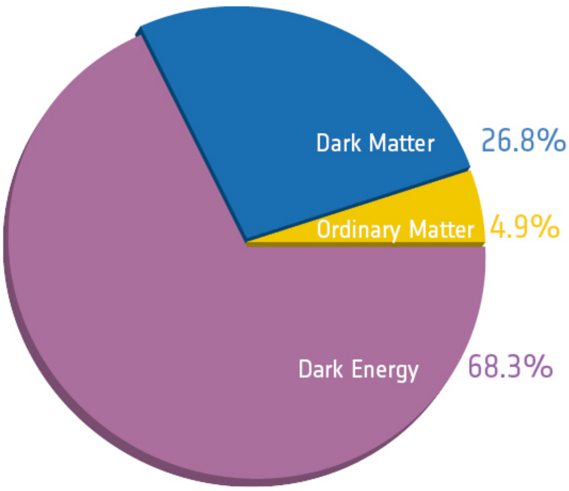

Figure 1.1: Composition of the universe based on Planck data [3].

Dark energy describes the repulsive force which accelerates the expansion of the universe. Dark Matter is a summary term for mass which cannot be seen directly, as it does not take part in the electromagnetic interaction. Its existence can be inferred from its interactions through the gravitational force, which makes the dark matter *visible* as mass [4]. There exists a variety of possible dark matter candidates; axions are one of them.

1.1 Axion theory

1.1.1 The strong CP problem

The CPT theorem, where C stands for charge conjugation, P for parity transformation and T for time reversal, states invariance of interactions when all three operations are applied [5, 6]. The experiment designed by Cronin and Fitch showed that the combination of C and P is violated in weak interactions using Kaon decays [7].

The strong interaction is described with quantum chromodynamics (QCD). One term in the QCD-Lagrangians violates CP-symmetry. It is displayed in eq. (1.1).

$$\mathcal{L}_{\not{CP}} = \theta \frac{\alpha_s}{8\pi} G^a_{\mu\nu} \tilde{G}^{\mu\nu}_a \tag{1.1}$$

This term implies for example a non-zero electric dipole moment of the neutron. However, this effect has not been found so far. The corresponding experiments were able to set an upper limit to the electric dipole moment of the neutron. The expected value was in the order of 10^{-13} e · cm, the current limit is in the order of 10^{-26} e · cm [8]. The missing electric dipole moment of the neutron gives the impression that CP symmetry is conserved for the strong interaction, although the theory allows violation of the symmetry and the electroweak interaction features CP-violation. The missing CP-violation for the strong interaction is called the *strong CP problem*.

One solution of the strong CP problem is to set the mass of one quark to zero. However, this solution has been excluded, leaving a θ constant of small value to be explained [9]. Peccei and Quinn proposed another solution, by exchanging the constant θ in eq. (1.1) with a variable proportional to $\frac{A(t,x)}{f_A}$, where A is the axion field and f_A the high energy scale at which the PQ-symmetry is spontaneously broken [9].

1.1.2 Axions

In quantum field theory a dynamic entity is a field, and each field comes with its particles. For the introduced field by Peccei and Quinn one of these particles is the axion [10]. The axion is a stable and light particle, for f_A is inversely related to all axion couplings as well as the axion mass [11, 9].

The vacuum realignment mechanism is one explanation for the axion and its mass. Here, the variable $\frac{A(t,x)}{f_A}$, exchanging the θ constant, evolves with time to zero. A visual explanation of the vacuum realignment mechanism is given in fig. 1.2. *Before PQ transition* refers to a time in the universe where the temperature was above f_A. There the field is a paraboloid. When the temperature drops below f_A the potential changes to a *Mexican hat* potential. The axion can be visualised as a particle moving on the line of the lowest potential. When the temperature decreases further falling below the QCD phase transition temperature (*after QCD transition* in fig. 1.2), the potential gets its tilt. The tilt gives the axion its mass, as the axion starts to oscillate around the minimum of the potential. This minimum is the preferred value of the field which at the same time is the value allowing for CP-symmetry of the strong interaction [9, 10]. The bottom right image in fig. 1.2 presents a tilted Mexican hat potential, which is deformed such that it additionally has local minima. This potential presents a more realistic axion potential taking into account additional effects, which are described in [9] with more detail. The oscillations around minima in the vacuum realignment mechanism fill space with axions, which then in turn correspond to cold dark matter. More details on axions as cold dark matter can be found in [9] and further information on ideas and concepts supporting the axion can be found in [11].

1.1.3 Primakoff effect

The axion-photon coupling $g_{a\gamma}$ follows from the PQ mechanism and is the most popular interaction mechanism for experimental axion searches [9]. One of the photons can be provided by a strong magnetic field, in order to trigger a conversion of the axion to a photon or from a photon to an axion. This conversion is called *Primakoff*-effect and the corresponding Feynman diagram can be found in fig. 1.3.

1.1.4 Solar axions

If axions exist, they are produced in the sun. The large abundance of photons and strong magnetic fields are good ingredients for the Primakoff-effect to take place. The axions could escape the sun, as they would not interact with the suns matter, in contrast to photons. The comparison of the solar neutrino flux with helioseismology as well as the suns lifetime allow to constrain axions [9]. The expected spectrum can be seen in fig. 1.4, with a maximum at around 3 keV, which corresponds to the energy of photons in the suns core.

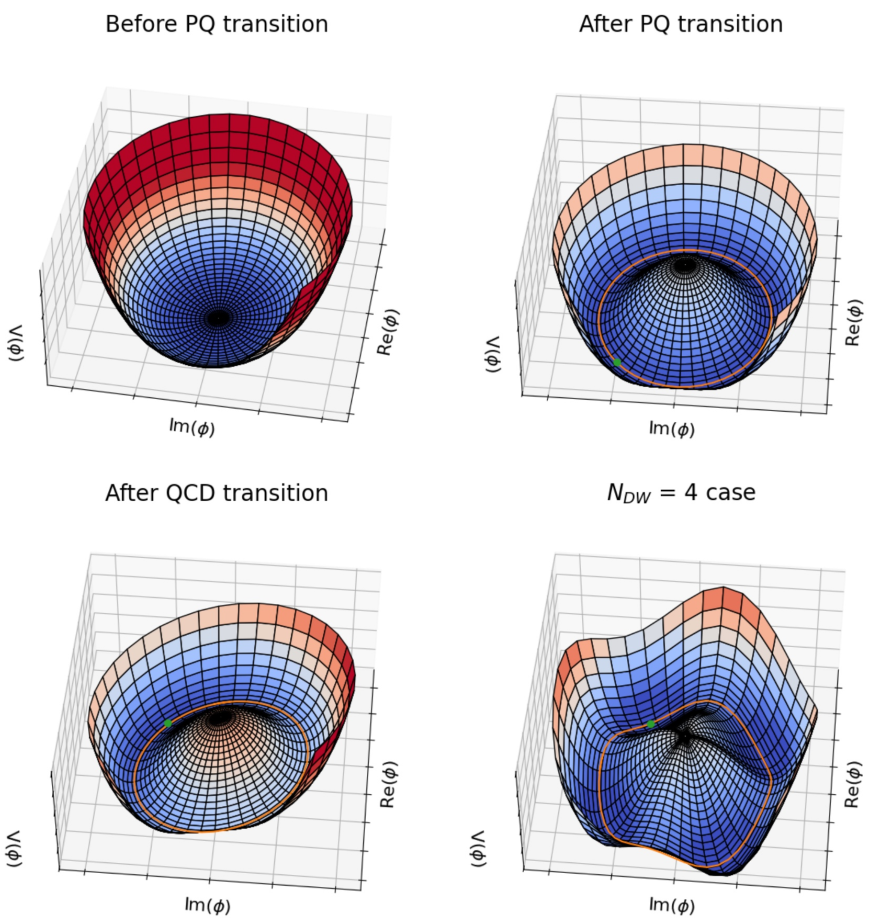

Figure 1.2: The vacuum realignment mechanism explains the evolution of the axion field. The mass of the axion can be understood as the oscillations in the axion field. The mechanism fills thereby the universe with cold dark matter axions. Figure taken from [9].

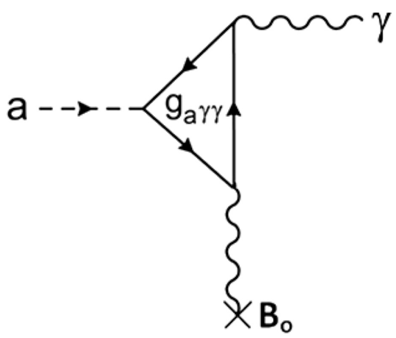

Figure 1.3: Feynman diagram of the Primakoff effect. A photon (γ) interacts with a strong magnetic field (B_0) and can be converted to an axion (a). Figure adapted from [12].

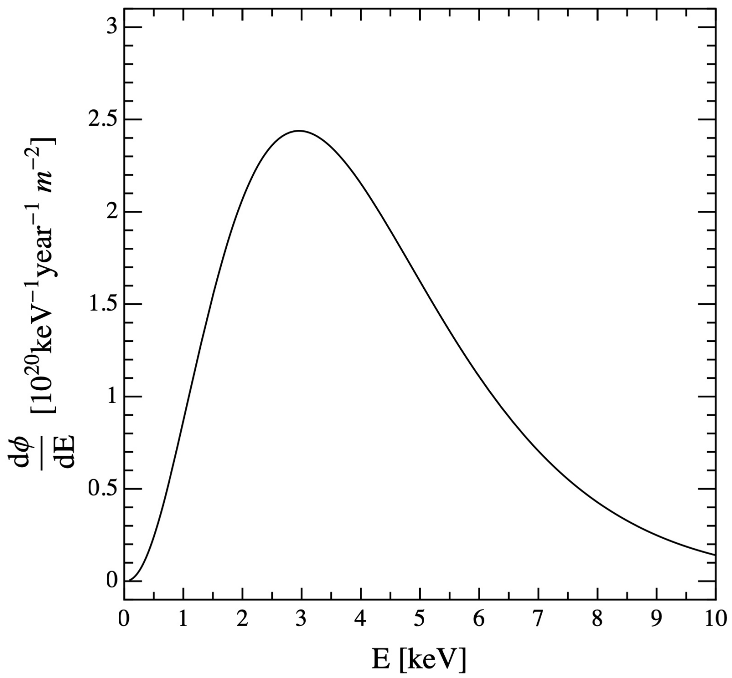

Figure 1.4: Solar axion spectrum with a peak at 3 keV. This energy corresponds to the energy of photons at the suns core, where the photons could be turned to axions with the Primakoff effect. For the spectrum a coupling constant $g_{a\gamma} = 10^{-12}\,\mathrm{GeV}^{-1}$ was chosen. Figure adapted from [9].

1.2 Axion detection methods

Most axion searches rely on the conversion channel mentioned in section 1.1.3. The experiments searching for axions can be divided in three groups, according to the origin of the axion.

- Haloscopes search for axions in the halo of our galaxy. These axions would be relic axions and part of the dark matter.
- Laboratory experiments, which search for axion-related phenomena, for example *light shining through a wall* (LSW) experiments like *ALPS*, create axions themselves.
- Helioscopes which search for axions produced in the sun.

The axion detectors are sensitive to a certain range of coupling and mass, and only if no signal is found, an exclusion is derived. Sensitivities and exclusion curves of different searches in terms of coupling strength and axion mass are shown in fig. 1.5. The coloured sections with solid lines have been probed by the corresponding experiments. Dashed lines indicate exclusion lines of future experiments. LSW and other laboratory experiments are in grey, helioscopes and stellar boundaries in blue, haloscopes and cosmological bounds in green and hinted region of QCD-axions in yellow.

1.2.1 Haloscopes

A haloscope typically consists of a tuneable microwave cavity in a magnetic field. The axions present in the halo of our galaxy can then be turned to photons, while traveling trough the experiment. Haloscopes work like radio receivers, such that if the frequency of their microwave cavity is tuned to the frequency of the axion field the haloscope can measure a signal. The matching frequency of the cavity enhances the conversion process [15]. The enhanced conversion leads to an increased signal strength. Haloscopes are very sensitive, however, their downside is that they can only probe a small parameter space at a time. Their sensitivity additionally depends on the fraction axions make up in dark matter. Another disadvantage is the complicated

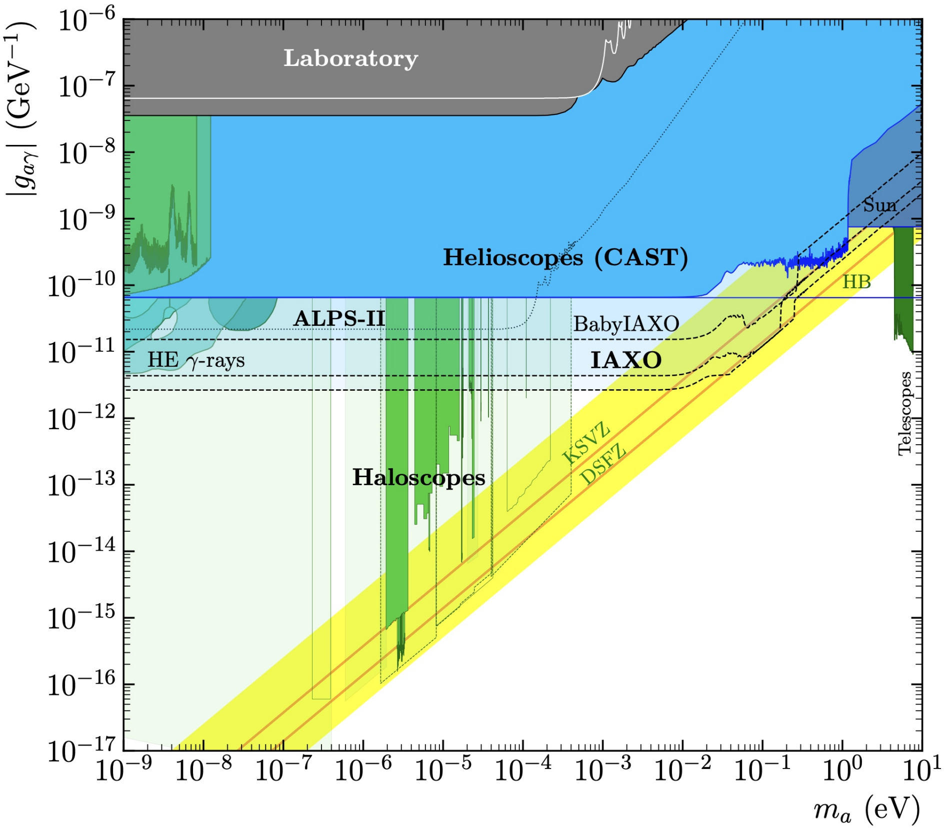

Figure 1.5: Axion parameter space with the expected sensitivities of BabyIAXO and IAXO. Helioscope and stellar boundaries are blue, haloscopes and cosmological bounds are green, LSW bounds are grey and the hinted region of QCD-axions is yellow. Current limits are solid lines, dashed lines are future sensitivities. Figure taken from [11]. Detailed explanations of the different exclusions can be found in [9, 13, 14]. Current constraints can be found in fig. A.1, with explanations in [14].

upscaling of haloscopes to reach new parameter space. Lower frequencies require larger cavities, higher frequencies smaller cavities. The problem of the small cavities is decreased signal and sensitivity [11, 9]. A sketch of a haloscope is given on the left side of fig. 1.6, with a sample signal on the right.

1.2.2 Laboratory experiments

Laboratory experiments, like *light-shining-through-walls* experiments (LSW), are not bound to assumptions regarding cosmology or astrophysics. Axions do not have to be dark matter for a LSW experiment, the only prerequisite is a $g_{a\gamma}$ coupling. They are called *laborartory experiments* because the axion particle is created in the

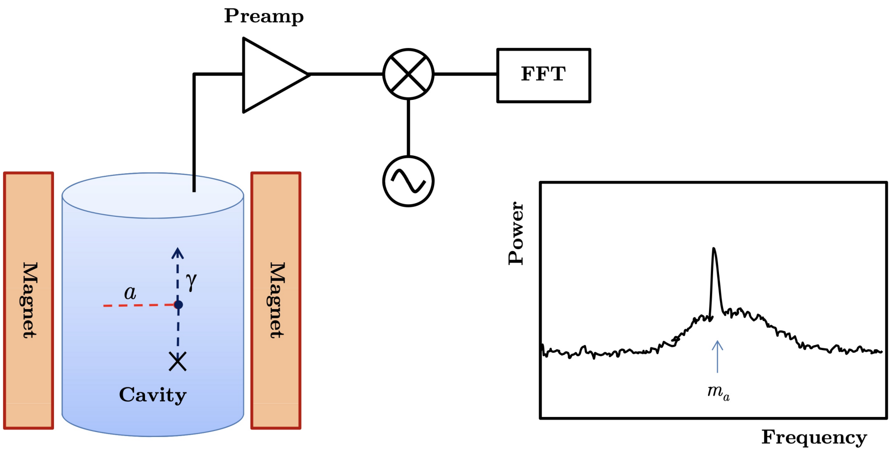

Figure 1.6: Sketch of a haloscope type, which in this case is a tuneable microwave cavity in a magnetic field. The frequency of the microwave cavity enhances axion to photon conversion if the microwave frequency is close to the frequency of the axion field [15]. The resulting enhanced signal allows to draw conclusions on the axion coupling to photons and its mass. On the right an example of an expected signal signature is shown [9]. Figure taken from [9].

experimental setup, in contrast to the other two types, which use already available axions. However, laboratory experiments, like LSW, are limited due to the low probability of the conversion taking place twice [11, 9]. One example of an LSW experiment is *ALPS*. The idea behind ALPS is to convert photons of a laser beam to axions with a strong magnet. These axions can then pass through a wall, and are converted back to photons with another strong magnet. These photons can then be detected [16]. Figure 1.7 shows the schematic setup of an LSW experiment.

1.2.3 Helioscopes

Helioscopes are using the same conversion concept as laboratory experiments. The first section of the laboratory experiments is outsourced to the sun. The large abundance of photons and strong fields make the sun a possible producer of axions. The Helioscope consists only of the second part of the laboratory experiment and turns the axions back to photons, as depicted in fig. 1.8. Like for the LSW experiment, axions do not have to be dark matter in order to be detected. The sensitivity of the helioscope is axion mass independent and the setup can be scaled up to reach unexplored parameter space [11, 9].

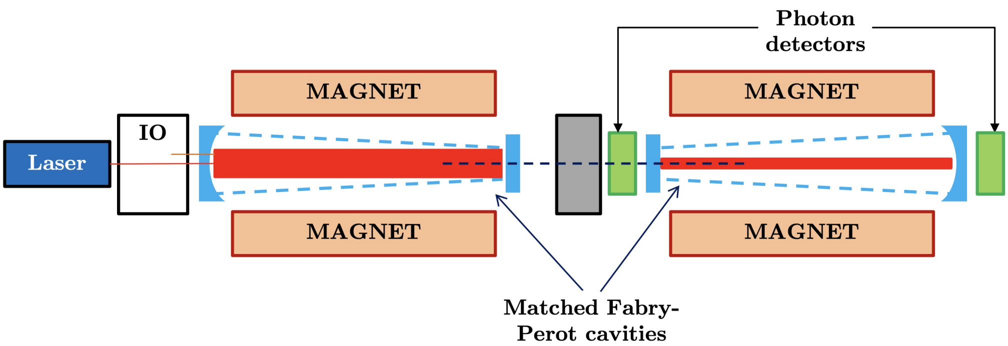

Figure 1.7: Sketch of an LSW setup. The laser light enters the Fabry-Perot cavity, which is surrounded by a magnet. A photon can be turned into an axion, pass through the wall in the centre of the sketch and enter the second cavity. There the axion can be turned back into a photon using the reverse effect from before. Figure taken from [9].

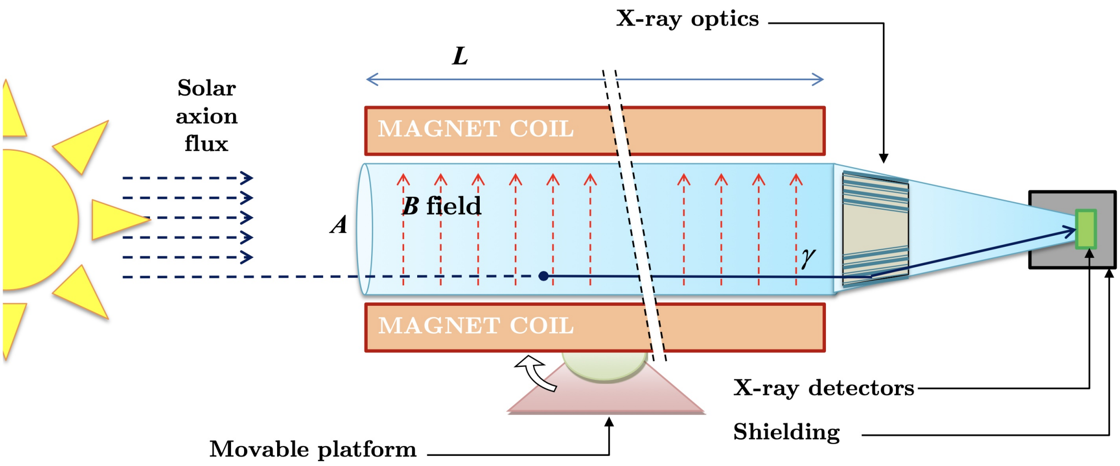

Figure 1.8: Axion helioscope sketch. The helioscope follows the sun. The axions (dashed lines) which originate from the sun travel through a strong magnetic field, which will convert some axions to X-ray photons (solid line) with the inverse Primakoff-effect. These X-ray photons are guided by X-ray optics to the detector. Figure taken from [9].

2 IAXO

The International Axion Observatory (IAXO) is a next-generation helioscope, which is going to look for solar axions and axion-like-particles (ALPs). It is a successor of the CAST experiment and its goal is to explore the parameter space further. The used effect will be, just like in CAST, the coupling between axions and photons - the so-called *inverse Primakoff-effect* [11], explained in section 1.1.3.

The axion converts to an X-ray of an energy of about 1 keV to 10 keV with the help of a strong magnet [11]. Compared with its predecessor CAST the IAXO helioscope will have an improved signal-to-noise ratio (SNR) by the factor 10^4. This is mainly achieved with a larger magnet, an improved detection efficiency and lower background [17, 11].

2.1 IAXO setup

IAXO will have a magnet with eight bores, each equipped with X-ray optics and a low-background detector. The magnet will be 20 m long with a field strength of 2.5 T [11]. At the end of the magnet X-ray optics will be placed, focusing the photons onto a detector. A visualisation concept is shown in fig. 2.1. The expected background is at 10^{-8} counts/keV/s/cm^2, reducing it by two magnitudes compared to CAST. The IAXO helioscope will be able to follow the sun over the course of the day for a duration of 12 h [9].

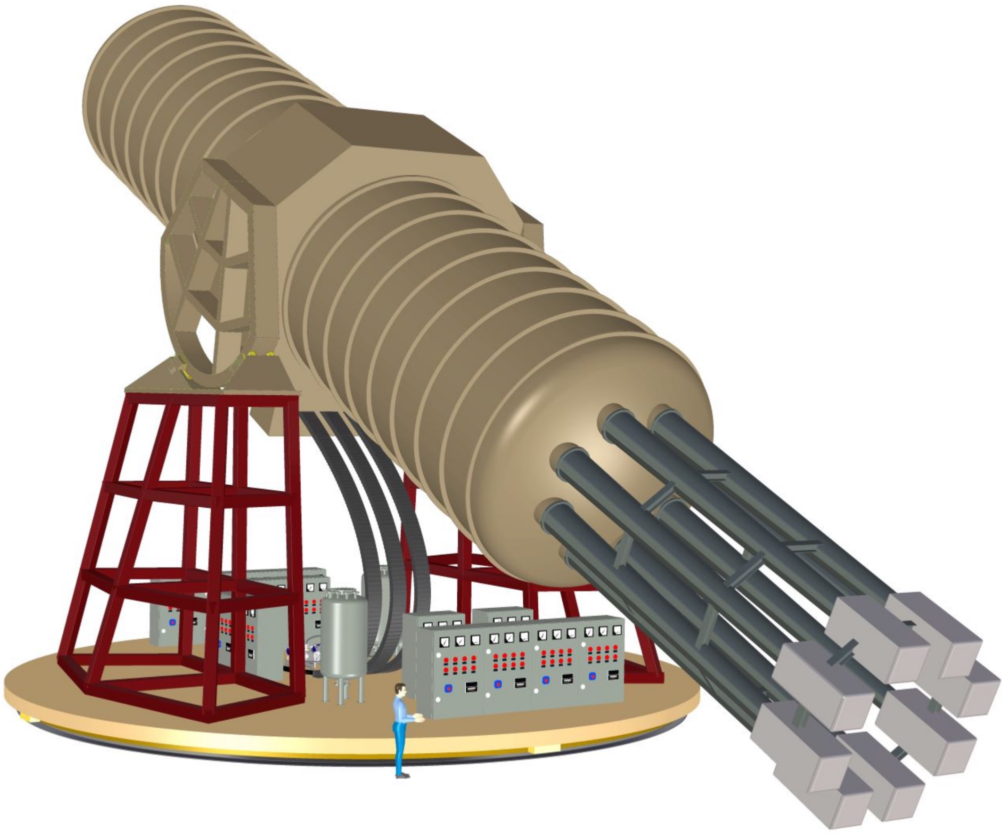

Figure 2.1: IAXO helioscope concept visualisation. The magnet is inside the brown cylinder which is mounted on a movable platform, which enables tilting and a horizontal movement, allowing the helioscope to follow the sun for 12 h per day. At the back of the cylinder the eight bores containing X-ray optics (dark grey cylinders) exit the magnet container with a detector each (light grey boxes) attached at their end. For better size estimation a human is depicted in front of the moving platform, where the control units are placed. Figure taken from [11].

2.2 BabyIAXO

In order to test components for IAXO, a smaller helioscope called BabyIAXO will be built first at DESY in the HERA south hall. BabyIAXO will probe an unexplored section of the parameter space and provide new information, beyond just being a test site for the subsystems of IAXO [11].
Figure 2.2 is a visualisation of the BabyIAXO helioscope. BabyIAXO will have two detection lines, where each detection line will have X-ray optics and a detector. The bores of the BabyIAXO magnet have a diameter of 70 cm. The magnet will be 10 m long with a field strength of 2 T [11].

The magnet is inside the brown cylinder with the two bores. The X-ray optics are the grey tubes in the back, with boxes attached to their ends. These boxes contain the detectors. In order to have axions travelling through the helioscope, the helioscope needs to follow the sun accurately through the day. Therefore, the setup is mounted on a moving platform. BabyIAXO will be able to probe the parameter space to a coupling of approximately $1.5 \times 10^{-11}\,\mathrm{GeV}^{-1}$ for the axion-photon coupling. The mass range will be up to 0.25 eV [11]. A detailed parameter space can be found in fig. 1.5.

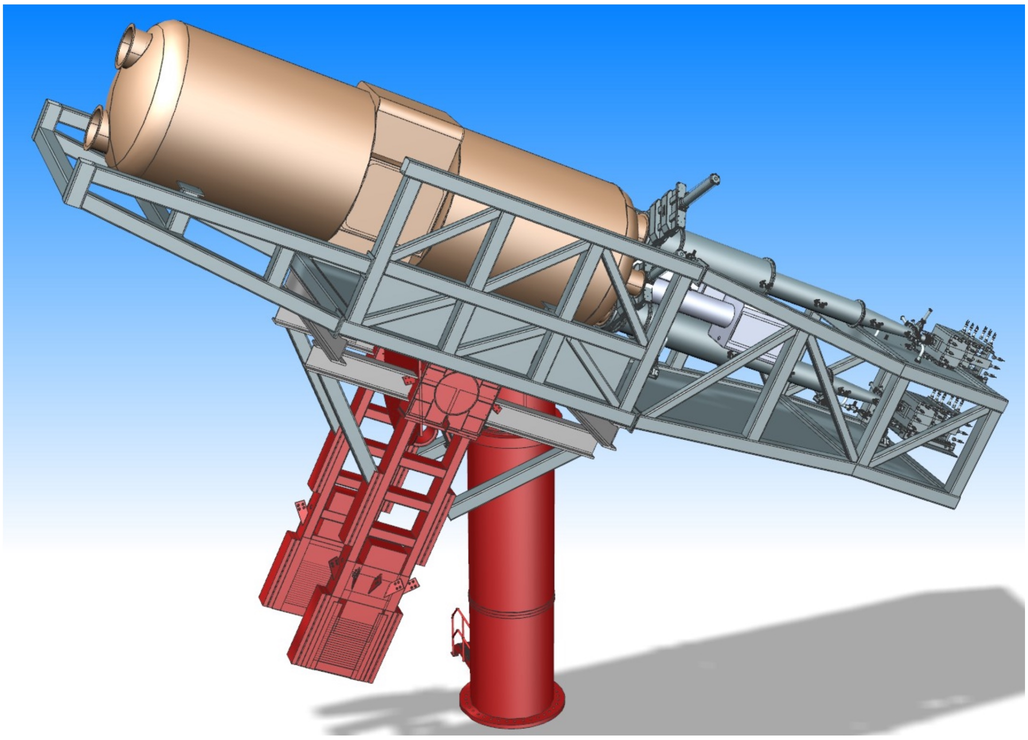

Figure 2.2: BabyIAXO helioscope visualisation. The magnet is inside the brown cylinder with the two bores. The X-ray optics are the grey tubes in the back, with boxes attached to their ends. These boxes contain the detectors. The magnet with the optics and detectors is mounted on a movable platform, enabling the magnet to follow the sun for 12 h a day. Figure taken from [11].

2.3 Requirements for the detector

The expected signal of the axion to photon conversion are X-rays in a range between 1 keV to 10 keV, where the targeted sensitivity requires to probe for single events per year [11]. The detection efficiency in the region of interest was ranging from 60 %

to 70 % for the detectors used in the CAST experiment. A high detection efficiency is desirable, as the expected event rate is low. The minimal detection efficiency is set to 70 % for BabyIAXO and 80 % for IAXO [11]. The required background rate is 10^{-7} counts/keV/s/cm^2 for BabyIAXO and 10^{-8} counts/keV/s/cm^2 for IAXO [11]. These limits are challenging and they have not been reached yet in the desired setting.

Energy resolution and low-energy threshold are a secondary requirement only. The threshold goal value is at least 1 keV [11]. The resolution and threshold play a role when searching for axions created by axion-electron coupling. Characteristics of this process are lower energies and a spectrum with monochromatic peaks [9].

3 TAXO

The BabyIAXO helioscope is a scaled-down version of the planned IAXO experiment. The purpose of BabyIAXO is to test and study possible components of the full-scale experiment, while exploring new parameter space. In order to be an eligible detector candidate for BabyIAXO, the X-ray detector needs to fulfil the requirements set in the BabyIAXO technical design report. One requirement is to have a background not exceeding 10^{-7} counts/keV/s/cm^2 for the range between 1 keV to 10 keV. The desired detector efficiency in the region of interest is set to 70 % with a threshold of 1 keV [11].

X-rays can be detected using a silicon drift detector (SDD). In this detector type charges are created when ionising radiation like X-rays, gammas or electrons hit the senstivive area. These charges are proportional to the deposited energy of the particle. With the application of an electric field these charges are guided to the anode, where they are read out. A sketch of an SDD pixel is shown in fig. 3.1. The pixel has an integrated FET, for amplification of the signal. Details on the drift behaviour of charge clouds can be found in [18].

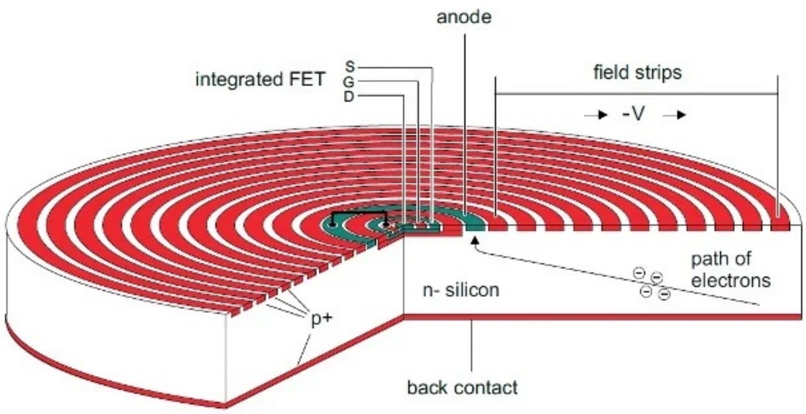

Figure 3.1: Example of a SDD-pixel design, taken from [19]. Charge clouds are guided by an electric field towards the centre where an integrated FET enhances the received signal.

The small band gap of the silicon semiconductor is source of a leakage current. This current is caused by thermally excited electrons, which are able to surpass the band gap. With increasing temperature this effect becomes stronger. Cooling of the detector reduces the thermal excitation and improves thereby the resolution. The

small band gap makes shielding against light necessary as well. A short overview about the physics of SDDs with more details can be found in [20].
After charge-sensitive amplification the SDD signal resembles a ramp, where the slope stems from the leakage current. Every time the amount of collected charges surpasses a given threshold, a reset pulse removes the collected charges. During the reset no signal can be recorded, which results in a small dead time for the detector. The charges created by an ionising particle are visible as a step on the ramp. Figure 3.2 displays schematically the recorded signal consisting of leakage current ramps and multiple particle interaction signals.

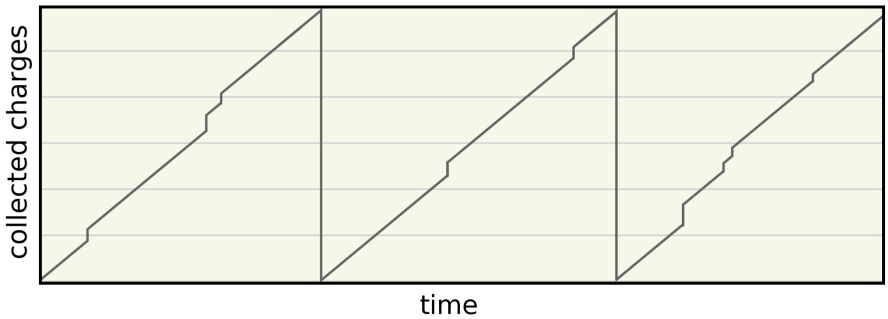

Figure 3.2: SDD first stage signal sketch. The ramps are caused by the leakage current. Ionising particles depositing energy in the SDD cause the steps in the ramp.

The TRISTAN SDD is a detector designed for the search for sterile neutrinos at the KATRIN experiment [21]. The detector is versatile due to its features and can be therefore used in other applications as well. The TRISTAN SDD used in this thesis consists of seven hexagonal pixels of 3 mm. An exemplary detector can be seen in fig. 3.3, which shows the readout side with numbered pixels corresponding to the channel numbers. The active area of the 7-pixel TRISTAN SDD is 0.41 cm^2.

Key features of this detector are a good energy resolution of less than 200 eV at 5.9 keV for photons at room temperature [18], a low threshold of 1 keV, linear behaviour deviating <0.1 % in the range from 6 keV to 60 keV [2], a high rate capability up to 10^5 cps [21], vacuum compatibility and cooling option to at least −30 °C [21] and a high detection efficiency of more than 95 % in the region of interest between 1 keV to 10 keV [23] (compare with fig. 3.4). More information on the TRISTAN SDD can be found in [21].

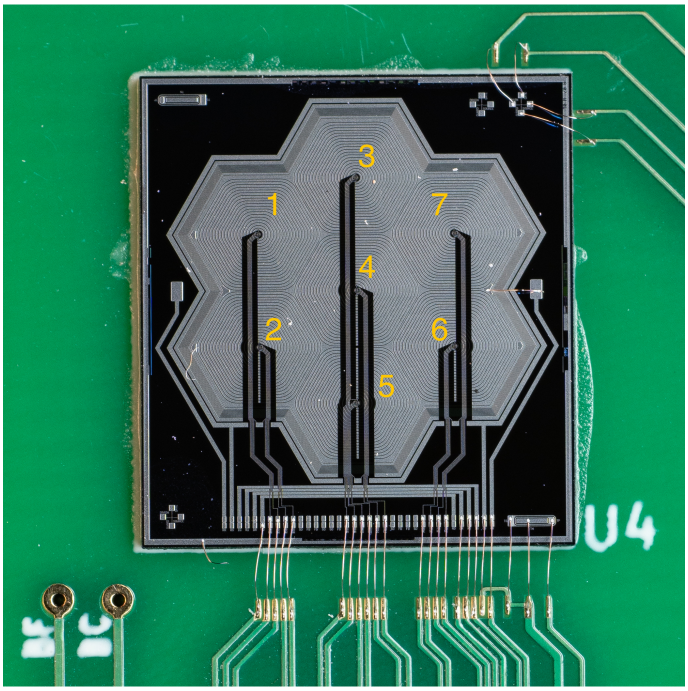

Figure 3.3: Seven pixel TRISTAN SDD depicted from the readout side. The individual pixels are identified with numbers from 1 to 7. Image adapted from [22].

With these features the TRISTAN SDD is a good candidate to fulfil requirements set for BabyIAXO and IAXO. The only not yet verified property is the background index, which is not a concern for the TRISTAN application. However, there is great potential for the SDD setup to not exceed the background limit. Due to the properties of Si radiopure production is possible and different shielding types can be applied around the setup. The exploration of the background index and its comparison to the desired value is the main goal of this thesis.

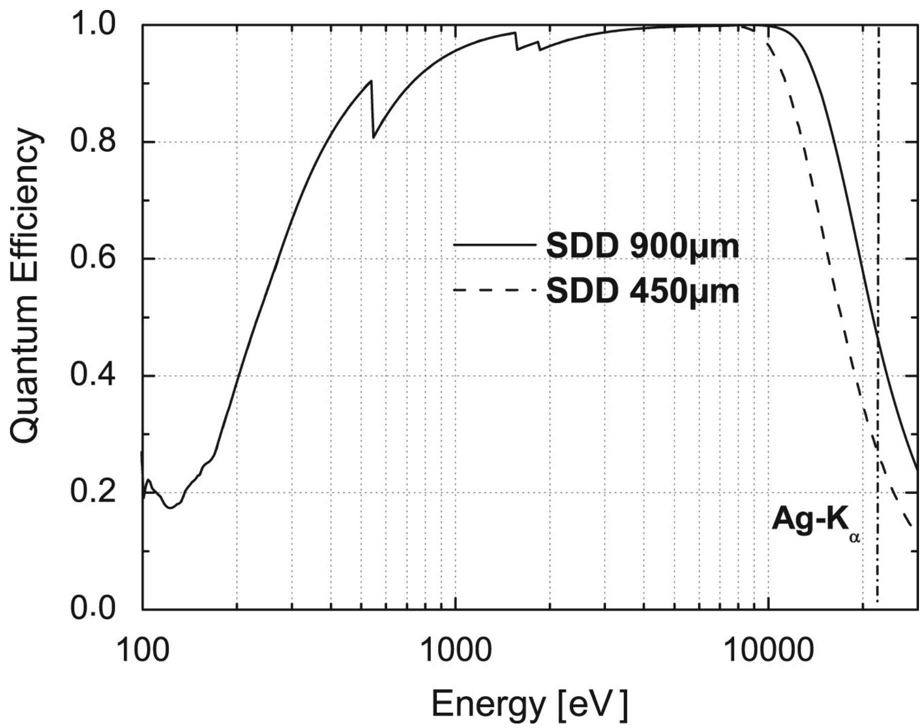

Figure 3.4: SDD detection efficiency. For the region of interest between 1 keV to 10 keV the detection efficiency lies above 95 %. Figure taken from [23].

3.1 TAXO SDD Demonstrator

As described in chapter 2, the IAXO experiment is a rare-event search and hence requires a low-background level. The low-background property is especially important for the detector part of IAXO. In order to verify if the TRISTAN SDD can fulfil the stringent background requirements a demonstration setup was built.

There are two sources of background: external and internal background. The internal background comes from the setup itself, like the SDD, the PCB or the readout electronics. In order to minimise the background of the setup the components need to be as radiopure as possible, and the parts containing radioactive components should be as far away as possible from the detector, with shielding in between them and the detector.
The detector used in the demonstration setup is a seven pixel TRISTAN detector. Originally designed without the low-background requirement, a custom PCB design was necessary to adapt for the changed use case of the TRISTAN SDD for a rare-event search. The electronics side with the application-specific integrated circuit (ASIC),

which is used to read out the signals, was identified to contain components, which are not radiopure. The distance between the detector and its readout electronics was therefore increased and the connection of these two section has no direct line of sight, due to a curved shape. The result is a custom PCB board with an ASIC part (*body*) with long connection lines (*neck*) to the SDD (*head*) with no direct line of sight in between. The board was named *Giraxo* as the long connection lines resembled the neck of a giraffe. The PCB board with the SDD used for the internal background measurement in the course of this thesis can be seen in fig. 3.5. A detailed description of the PCB board development and design can be found in [22].

The Si wafer used for the SDD of the demonstration setup was tested for radiopurity. The material of the PCB board, where the SDD is placed on, and the glue were both chosen based on their radiopurity.

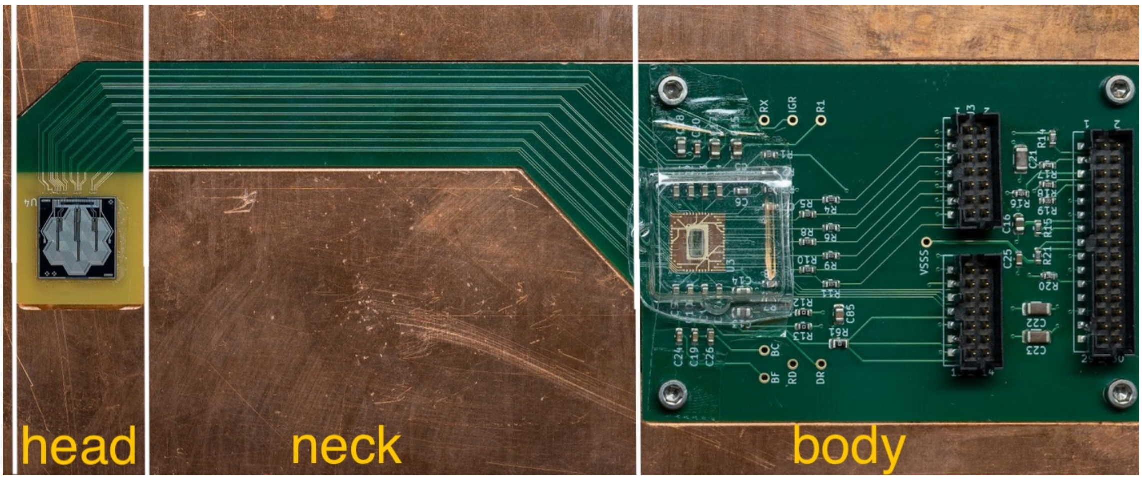

Figure 3.5: Custom PCB design (*Giraxo*) for the TRISTAN SDD, where the readout electronics and the detector chip are connected with elongated connection lines without a direct line of sight. The Giraxo-PCB lies in a copper holder to shield the chip from the potentially more radioactive electronics section of the board.

In order to measure the remaining internal background the external radiation needs to be prevented from reaching the detector. External background can have cosmic origin or come from radioactive decay close by the setup. The onion shell structure of the TAXO SDD demonstrator is build to prevent these external sources from reaching the detector.

Cosmic ray background can be reduced by the overburden of an underground laboratory. To test the internal background, the experiment was located at the Laboratorio

Subterráneo Canfranc (LSC) in Canfranc (Spain), which is an underground laboratory located underneath a mountain, with a water equivalent of 2400m [24] - see fig. 3.6.

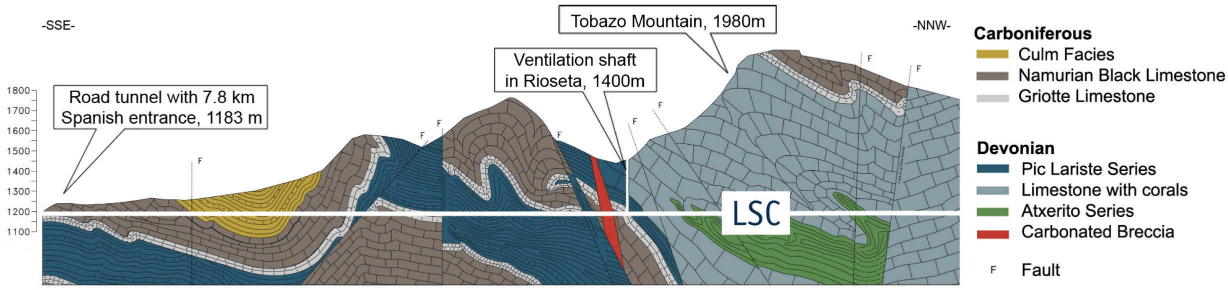

Figure 3.6: Longitudinal geological profile of the mountains above LSC. Figure taken from [25].

A common source of background is Radon in ambient air. To prevent Radon gas, which would lead to an additional background, the setup is inside a nitrogen flush box.
Inside the flush box the TAXO SDD on its Giraxo-PCB is packed into a lead castle with walls of 10 cm. To shield potential ^{214}Pb gamma radiation of 47 keV, there is a Cu layer of at least 1 cm made from cleaned radiopure copper. Cu has a prominent fluorescence line at 8 keV [26], which in turn can be shielded by a Si layer of 1 mm (compare with fig. 3.7).

The design of the shielding with all its layers can be seen in fig. 3.8, where figs. 3.8a and 3.8c show the outer part that hosts the PCB as a sketch and photo respectively. In figs. 3.8b and 3.8d the inner layers are depicted as a sketch and a photo.

The BabyIAXO setup will be located in a shallow underground lab. There cosmic rays will be able to reach the detector. The solution will be a plastic scintillator muon veto and neutron shield. They will allow to identify muons, which gives the possibility to remove their signal from the data.

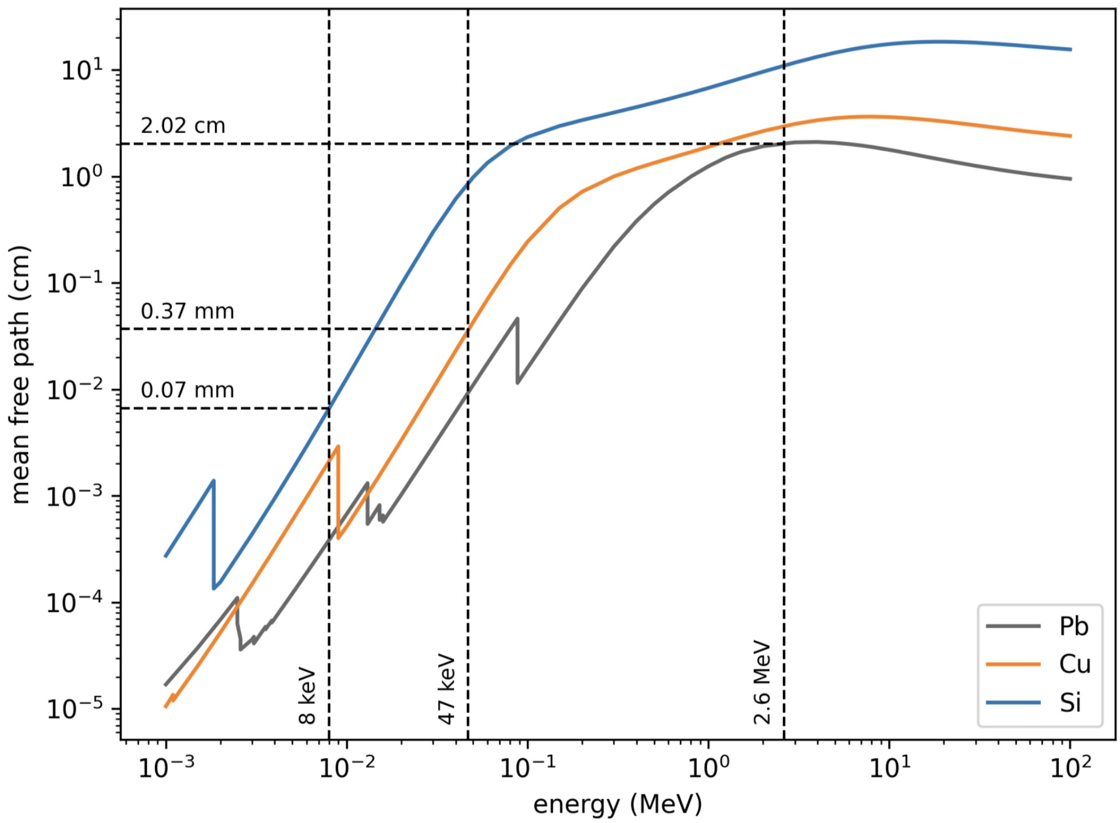

Figure 3.7: Mean free path of photons in Pb, Cu and Si. Figure courtesy of C.Wiesinger [27].

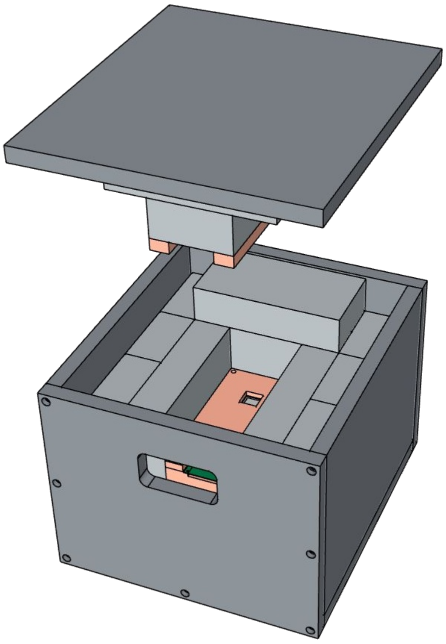

(a) A visualisation of the TAXO SDD demonstrator. The custom PCB with the detector is inside the copper block. The copper block of the size of a standard lead brick lies inside a lead castle, which is inside a nitrogen flush box. Figure courtesy of C. Wiesinger [27].

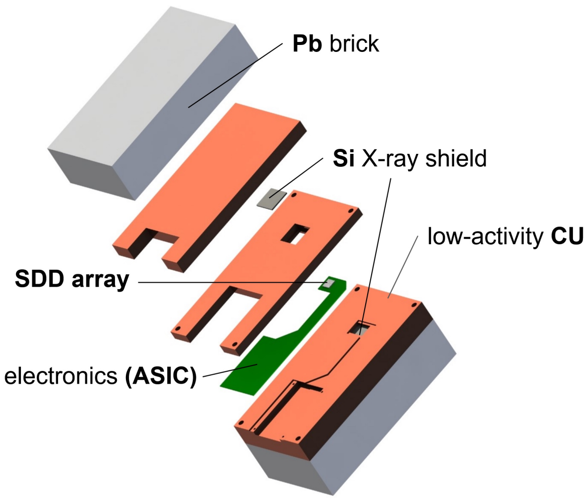

(b) Fanned visualisation of the copper block housing the Giraxo PCB board. The bottom part of the three layered Cu block holds the PCB and has a Si wafer to shield the SDD from below. The PCB is covered with a second Cu layer including another Si wafer to shield the SDD array from the top and from the electronics. The third Cu layer covers the entire PCD board. Figure taken from [22].

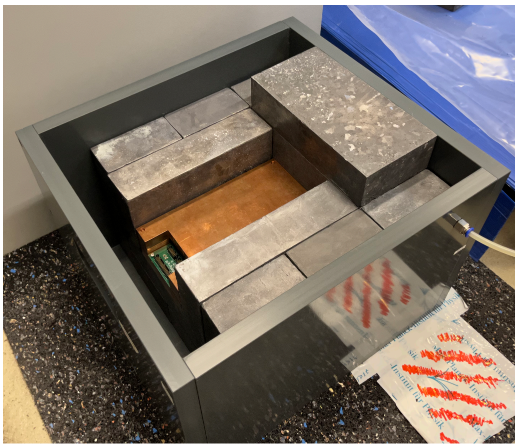

(c) TAXO Demonstrator.

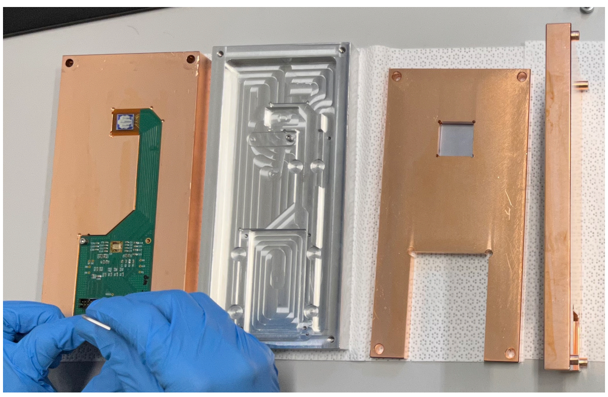

(d) Assembly of the Giraxo PCB in its Si-Cu shielding.

Figure 3.8: Passive shielding of the TAXO demonstrator setup. On the the left side the opened flushbox with the lead castle, with the copper brick containing the GIRAXO-PCB. On the right side the fanned copper brick with the Si shielding and the PCB is visible.

3.2 Electronics chain and data acquisition

The electronics chain of the SDD demonstrator consists of several parts. A graphical overview is given in fig. 3.9, the actual setup at LSC can be seen in fig. 3.10.

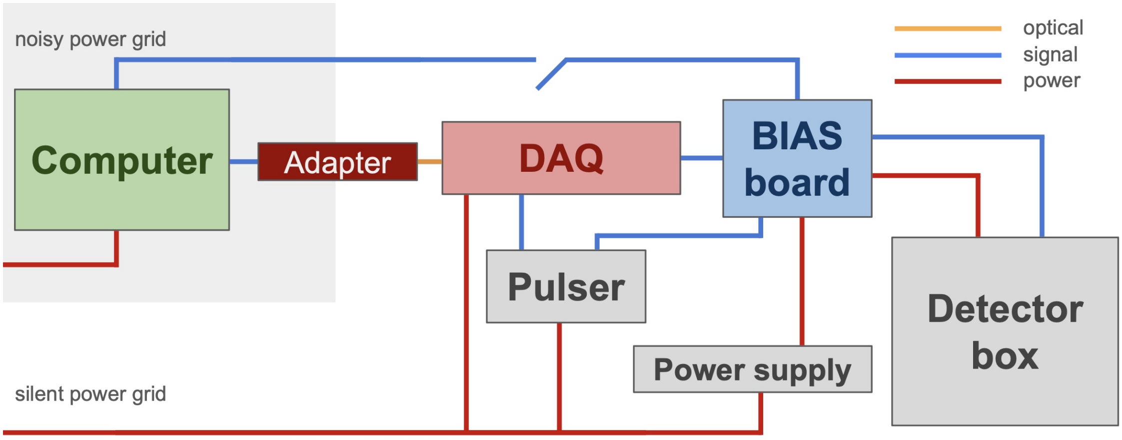

Figure 3.9: Sketch of the wiring of the TAXO Demonstrator. In red power lines, in blue signal lines. Optical fibre in orange. The optical fibre connection makes it possible to have the computer on a noisy power line, whereas the detector and the readout system is on a silent power line with less noise.

The SDD on the PCB is connected to a bias board designed by XGLab. This board performs a second stage amplification, which produces pulses with an exponential decay. Examples can be seen in fig. 5.1. These signals are sent to a CAEN V1782 DAQ board. The CAEN DAQ converts the analog signals to digital signals. The CAEN DAQ is controlled through the *CoMPASS* software on the computer. With this software the acquisition mode can be set and the data recorded by the SDD can be monitored in real time. The sampling rate was 100 MHz, with 4000 samples, resulting in a recording of 40 µs length. The pre-trigger time was set to 20 µs, such that the rising edge is in the centre of the recording.

The data was recorded in waveform mode. The CAEN DAQ receives signals from the seven SDD pixels (see fig. 3.3) and an additional pulser. Each time one of the channels records a signal, which is defined by the incoming signal surpassing a threshold, a full trace is recorded for each channel. This recording method is called a *global trigger*. The record of the waveforms from eight channels, consisting of seven pixels and the pulser, is called an *event*.

Figure 3.10: The TAXO demonstrator setup at LSC.

The background measurement requires a long runtime. The challenge of a long running measurement with only a few counts is to ensure stability. An inactive pixel can be missed, suggesting incorrectly the recording of a lower background. In order to enable monitoring of the entire measurement a pulser was included in the setup. The pulser was fed into the readout of the pixels, such that the pulser signal is visible in each channel. In case a pixel would have stopped working, the pulser signal would have vanished for this pixel.
The SDD is calibrated once. The pulser was included in the calibration in order to establish a relationship between the pulser position and the pulser energy. In case of changed bias voltages the pulser position would have a position shift. The pulser checks that all seven pixels are working and monitors the stability of the gain. With this monitoring method error sources of the long measurement time can be mitigated. Evaluation of the pulser stability can be found in section 5.1.1.

3.3 Data processing

The data recorded during the calibration and the background measurement is processed after the data taking. Each channel is read out individually, where a timestamp, which works as an identification number, and the waveform is saved. The analysis was performed in four processing steps that populate different data tiers:

0. DAQ data: CAEN DAQ card records data as binary files.

1. Raw data: binary data is converted to `hdf5` files. The bit encoding is described in the CAEN manual.

2. Digital signal processing (dsp) data: parameters are extracted from the waveforms. For this the following steps are performed:

   - baseline reconstruction, which is the flat part before the pulse, using the first 1024 datapoints. Here the *baseline average* and the spread of the baseline values (*baseline sigma*) are determined.

   - pole zero correction is applied to compensate the exponential decay of the signal, with a decay time of 1400 datapoints for pulses in pixels and 10,000 datapoints for pulses of the pulser. This correction turns the decaying signal into a step.

   - fast trapezoidal shaping and leading edge triggering, to determine the *triggers* and their positions.

   - trapezoidal filtering, for *amplitude* reconstruction. The amplitude is proportional to the energy deposited in the pixel of the SDD.

   The result is a file including the baseline, the baseline sigma, a trigger list, amplitude value for each trigger and a timestamp.

3. Calibrated data (cal): dataset with energies. The calibration functions are applied to the amplitudes in ADC units to get the energy in keV. The cal-file

contains the timestamp, the energy calculated with calibration functions from the amplitude value and a two bit flag. The zeroth bit is set when there is more than one trigger value, the first bit is set if the baseline sigma is higher than a set threshold. This flag is a quality cut and more about this quality cut can be found in section 5.2.2.

4. Event data: information gained in the previous steps is combined for waveforms of the same timestamp. Each time one of the pixels registered a pulse or the pulser sent out a signal, all channels were saved in an individual file. Calibrated waveforms with identical timestamps are combined to one event. The event file contains the timestamp for identification, a flag informing how many channels registered a non-zero energy, an array of the energies for all used channels, the multiplicity, the total energy and another flag informing whether the pulse came from the pulser. The energy reconstruction leads to values below zero as well. Negative values were set to zero. The multiplicity value counts all energy values above 0.5 keV. And only energies above 0.5 keV contribute to the total energy value. Energies below 0.5 keV are treated as noise signals.

The final step is to apply quality cuts to the events, as not all events qualify for the background data evaluation. The quality cuts are explained in chapter 5.

3.4 Measurement description

The determination of the background level of the TAXO demonstrator provides insight into the state and the limits of the current design. The value of the internal background will provide information on how close the TRISTAN SDD demonstrator is to the desired background index of 10^{-7} counts/keV/s/cm^2. Ideally the determination of the background index value is accompanied by spectral information, which can help to identify possible sources of the remaining background.

The total background measurement was divided in three sections. The first section was a test of the setup. The second step of the background measurement, after a successful test, is the energy calibration of the detector. The default output of an SDD pixel is an ADC value. By measuring characteristic lines in the spectrum of a radioactive source, energy values can be assigned to ADC values. Each pixel

has slightly different calibration values. The calibration performed in this thesis is described in detail in chapter 4.
After the calibration measurement the radioactive source is removed and the background measurement can be started as the third section. The background measurement uses the exact same setup as the energy calibration. With the applied shielding, described in section 3.1, the SDD records only the internal background. The measurement time to gather sufficient data for determining the background index was estimated with three months [28].

The measurement is divided into runs for technical reasons and the runs are named *runXXX*. Smaller datasets make an analysis easier. For each run the pulser was restarted and the settings of the bias system and the CoMPASS software were checked. This was necessary in order to check whether the components were still on and working with the desired settings.
Each run consists of events, where each event is assigned an individual timestamp which works as the identification number. An event consists of eight waveforms of the same length, one pulser signal and seven pixel signals.

After the first two runs (run001 and run002) the PCB was changed as a large noise signal was observed, and a second board was tested. The increased noise was not present in the second board, which was then used in all following measurements. The energy calibration run of the second PCB is run003. The numbering was not readjusted in order to maintain a consistent naming and to avoid confusion during the processing at a later point in time. The settings of the pulser, bias board and the CoMPASS software can be found in appendix B.
During the data analysis run004 and run019 turned out to have features which excluded them from direct use and are therefore not included in the figures of chapter 5. The application of dedicated quality cuts, described in section 5.2, removed the faulty data. Run004 and run019 could then be included in the final analysis steps as well as the background index estimation.

4 Calibration

The determination of the background spectrum of the TAXO SDD demonstrator requires an accurate reconstruction of the event energy. The DAQ-unit used in the setup, described in section 3.1, returns an arbitrary ADC unit, which can be related to the true event energy. Within the scope of this work, an Americium 241 (^{241}Am) source was used to calibrate the detector. In a subsequent campaign at the Canfranc Underground Lab (LSC), the unchanged setup was used to record a background spectrum to determine the background index. This calibration procedure relies on findings and resources as described in [2].

4.1 Spectral peak selection

The first step in the energy calibration procedure is to relate the spectral peaks in the measured spectrum to the theoretical lines of the ^{241}Am energy spectrum. In theory, the ^{241}Am spectrum has more than 10 identifiable peaks over a wide energy range (>50 keV) (see table C.1). A large energy range verifies the linear behaviour of the detector. The more spectral peaks are used the more accurate the fit. A feature of the SDD is a thin dead layer of about 10 nm at the entrance window [21], where deposited energy is only detected partially. The peaks of the ^{241}Am spectrum up to 60 keV are X-ray and gamma peaks. Photon detection is not impacted by the dead layer of the SDD, as photons have a high penetration depth. Therefore, low-energy peaks can be included in the calibration, making ^{241}Am a suitable calibration source.

The ^{241}Am spectrum was recorded for forty minutes, with the source at an activity of approximately 40 kBq and in close distance to the detector. Forty minutes was sufficiently long to obtain enough prominent spectral peaks for calibration purposes. In general, a longer acquisition time is recommended, to gather more data, reduce thereby the statistical uncertainty and make the spectral peaks easier to distinguish.

For choosing which of the measured spectral peaks should be included in the calibration, the selection scheme of [2] is used. A selection number ranging from 1 to 7 is assigned to peaks in the ^{241}Am spectrum. With increasing selection number the acquired spectral peak position approximated by a Gaussian distribution resembles

less and less the true position of the underlying peak. More details on the deviation can be found in [2].
The recorded spectrum of ^{241}Am in fig. 4.1 has three spectral peaks from the first, optimal selection. They are gamma peaks. However, only two peaks have a distinct, gaussian-shaped spectral peak. The remaining gamma peak is of low intensity and has too few counts to be used in the calibration. Two peaks are sufficient to fit a linear function, however, more data points make the fit more reliable. Therefore, peaks of selection numbers six and seven are included in the calibration as well (there were no usable spectral peaks of other selection numbers).
Spectral features with higher selection numbers are in general unsuitable for precise calibration [2]. As the main goal of this thesis is to determine the background of the detector setup and calculate the corresponding background index, the associated uncertainty in the linear fit can be accepted.

An example of the measured uncalibrated energy spectrum of ^{241}Am of one of the detector pixels (channel 06) is shown in fig. 4.1. Prominent spectral peaks are assigned a letter and the colour bands show the respective data range that is used in the Gaussian fit to determine the position and the width, which corresponds to the resolution, of the selected spectral peak (see section 4.3). Each channel of the detector has a distinct energy scale and requires a separate calibration.

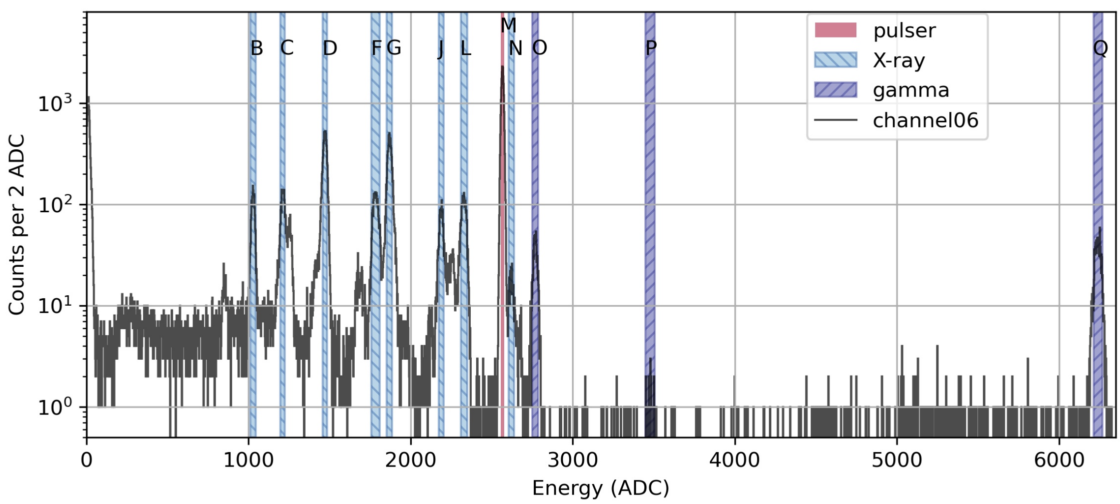

Figure 4.1: Uncalibrated energy spectrum (channel 06) measured in the presence of an ^{241}Am calibration source close to the detector. The most prominent spectral peaks have been assigned a letter each. The colour band shows the data range of the peaks used for fitting a Gaussian distribution to obtain the position and the width.

4.2 Peak identification

Each spectral peak is assigned a number in [2]. The ^{241}Am spectrum of this calibration run was graphically overlayed with the numbered spectrum from [2]. Thereby, spectral peaks from this calibration run were identified with spectral peaks in the numbered spectrum and given a letter. Some peaks in the numbered energy spectrum are superpositions of lines lying so close to each other that they cannot be resolved. In case such a peak agreed with the position of the spectral peak in the measured spectrum, the energy of the most intense peak was selected. The highlighted spectral peaks in fig. 4.1 are summarised in table 4.1, where the peak number and energy is given. More details can be found in the appendix in table C.2. Initially, more spectral peaks were identified. During the calibration process some spectral peak turned out to be unsuitable for some channels; they merged with larger spectral peaks close by or vanished in the surrounding noise. The calibration uses the same spectral peaks for all channels. Therefore, only spectral peaks were selected which were distinguishable in all channels. These remaining spectral peaks were not renamed, but kept the letter which was assigned to them in the beginning.
Table C.1 contains an overview of theoretically observable lines in the ^{241}Am spectrum. Neither the spectrum measured in [2] nor the spectrum measured during this thesis are ideal depictions of the theoretical spectrum. Due to line widths and noise not all lines are visible, especially lines of lower intensities, which vanish and lines with too little distance, which become indistinguishable and appear as one spectral peak. According to [29], the intensities of spectral peaks of the recorded spectrum can differ due to the source. The source can be packed in different materials, which can be seen by additional element specific peaks not associated with ^{241}Am.

The peaks in a measured energy spectrum can be sorted by their calibration qualities which are called *selections*, see table 4.1. A detailed description of the selection categories can be found in [2]. A low selection number means that the position of the spectral peak obtained with a Gaussian fit is close to the actual position of the corresponding peak. Higher selection numbers contain spectral peaks consisting of overlapping peaks or spectral peaks within non-negligible background contributions in the selected fit range. For these cases, a simple Gaussian fit returns a position which is farther away from the actual position of the main peak in the spectral peak. The fit can be improved by using modified Gaussian curves. For this thesis the uncertainty of the fitted peak position caused by using the simple Gaussian is acceptable.

The recorded spectrum in fig. 4.1 contains spectral peaks from four selections:

- selection 1 with distinct and single peaks, where the noise is negligible: O, Q, and M.
- selection 4 with spectral peaks consisting of two lines: B.
- selection 6 with higher, distinguishable peaks in merged features consisting of two or more lines: C, D, G, J and L.
- selection 7 with all remaining peaks: F and N

Spectral peak P was identified as a photon peak of selection 1 in [2]. The short measurement time of the ^{241}Am spectrum used in this calibration leads to a count number of P of less than 10. The spectral peak has in this case no Gaussian shape and cannot be used for calibration purposes.

spectral peak name	peak number	energy in (keV)	selection
C	12e	11.400	6
D	16b	13.964	6
F	20b	16.816	6
G	21b	17.751	6
J	24a	20.784	6
L	26a	22.220	7
O	28	26.345	1
Q	37b	59.541	1

Table 4.1: Overview of the selected spectral peaks of the measured ^{241}Am spectrum with the true energy, peak number (see number in table C.1) and selection number (adapted from [2]). A good candidate for calibration has a low selection number. With increasing selection value the mean of the Gaussian fit will describe less precisely the actual position of the peak. The pulser peak M cannot be used for the calibration. A more detailed description of the spectral peaks is given in the appendix in table C.2.

4.3 Calibration functions

After the selection and identification of the spectral peaks, a Gaussian distribution (see eq. (4.1)) is fitted to the peaks of the measured ^{241}Am energy spectrum. From the fit, the mean as well as the standard deviation are extracted.

$$f(x) = \frac{1}{\sqrt{2\pi\sigma}} e^{-\frac{1}{2}\frac{(x-\mu)^2}{\sigma}} \tag{4.1}$$

An example where a Gaussian is fitted to spectral peak Q can be seen in fig. 4.2.

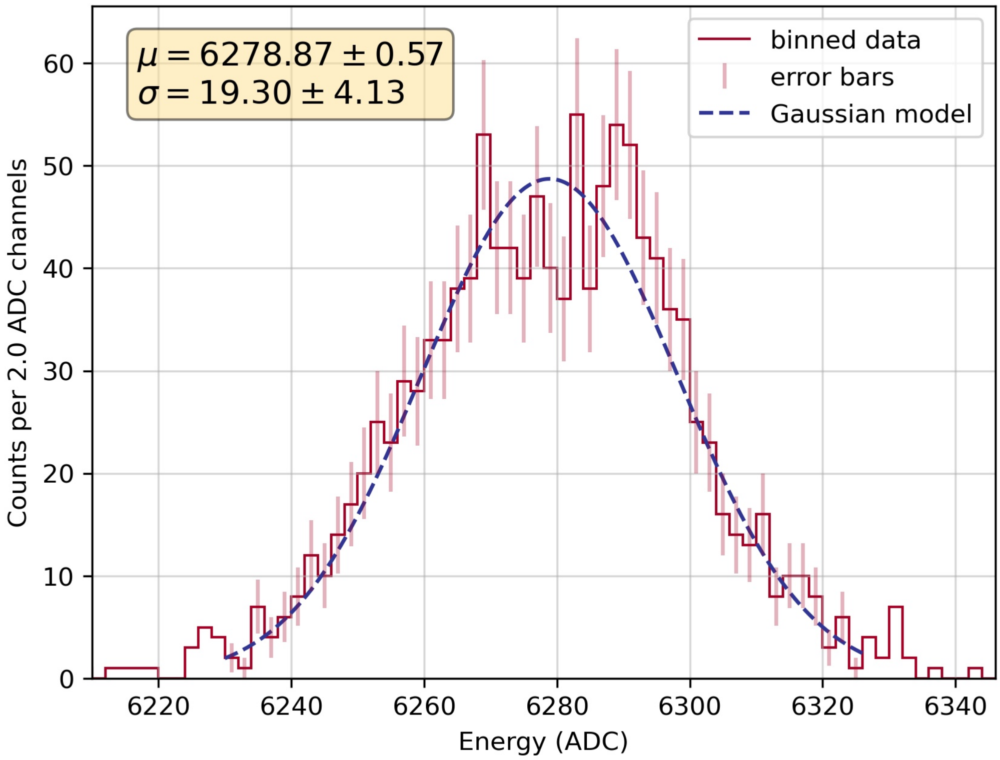

Figure 4.2: Fit of a Gaussian distribution (dashed line) to the measured peak Q (solid line) for an exemplary detector channel (channel 02), including the uncertainty ($\sqrt{N}$) (solid vertical lines) in the counts. The mean of the Gaussian is at 6279 ADC corresponding to an energy value of 59.5 keV. A good agreement of the peak with the Gaussian model can be observed.

Each detector channel has an individual set {ADC energy, true energy} of ADC values for the spectral peak positions, determined by the Gaussian fits, and true energy values of the spectral peaks. Applying a linear fit to the set returns a calibration function for each channel [21]. The set of fit points is the same for all channels and composed of eight spectral peaks, which can be found in table 4.1.

An example of the energy calibration for the measurement with an ^{241}Am source is shown in fig. 4.3. The first subplot shows the calibration data as well as a linear fit. The error bars are enlarged by a factor of 20 to increase visibility. The lower plot shows the residuals of the linear fit in eV (to be compared with the absolute values in table 4.1). All fit points have a deviation of less than 100 eV, which is better than the resolution of the peaks (see section 4.4). The fit functions with the respective subplots of all other channels can be found in appendix D.1. They contain the residuals in sigma and in percentage as well.

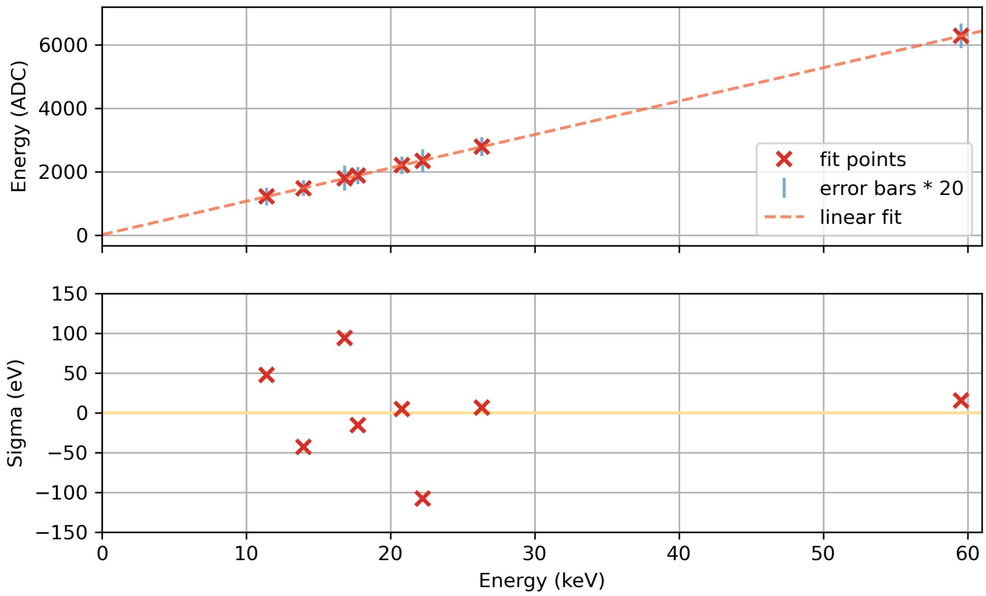

Figure 4.3: Energy calibration of a measurement with an ^{241}Am source (channel 02). The upper plot shows the peak position value as a linear function of the true energy. The lower plot shows the residuals, converted to eV. The datapoints fit well to the assumed linear relation. The deviation of the fit points is randomly distributed, with highlighted zero value for easier identification, and below 100 eV.

The obtained fit parameters of the linear fits of all channels are shown in fig. 4.4. Channel 01 has an offset of −200 eV and slope of 9.2 eV/ADC. All other channels have an offset between −170 eV and −140 eV and a slope within (9.5 ± 0.1) eV/ADC. The exact values including the uncertainties can be found in the appendix in table D.1.

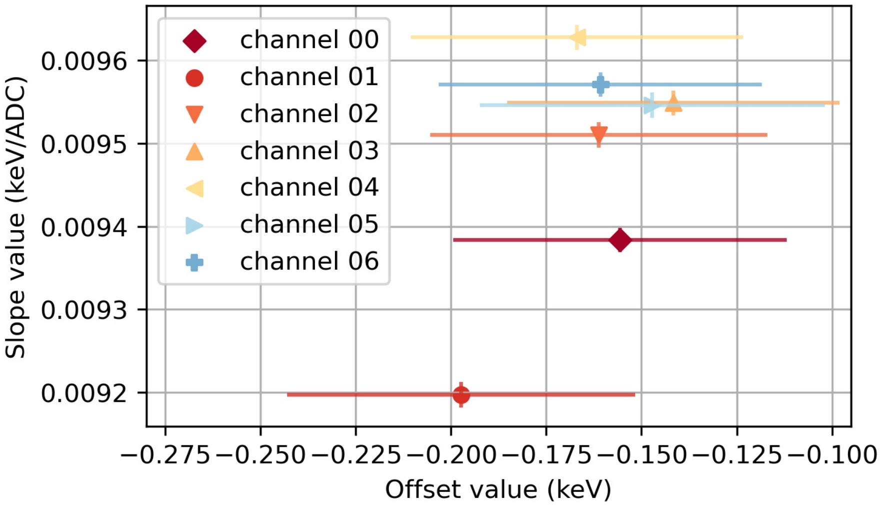

Figure 4.4: Slope and offset of each channel obtained in the energy calibration. Compared to the other channels, channel 01 shows a slightly different offset value, which, however, is compatible within the uncertainties with the other offset values. The slope values are very similar as well.

The values of the linear fits presented in this chapter contain a small error. There was a typo in the energy of one spectral peak (C). The actual energy should have been 11.242 keV instead of 11.400 keV. In addition spectral peak B could be included. Including these two changes has mainly an impact on the low-energy range. Here, the error in energy accounts for about 50 eV, which is significantly lower than the resolution of more than 200 eV for 0 keV (compare with fig. 4.7). An update of the energy calibration would have required a reprocessing of the background data and the related analyses. As this imprecision was discovered at a late stage during this thesis, it was decided to neglect the small bias due to limited time. An example for the corrected calibration fit including spectral peak B and the correct energy for spectral peak C can be found in the appendix in appendix D.2.

After having applied the energy calibration to the measurement data of the ^{241}Am spectrum, a calibrated spectrum as shown in fig. 4.5 is obtained. The respective calibration function was applied to each channel and the energy spectra of all channels were combined into a single, high-statistics spectrum by stacking the individual spectra. The necessary condition to be able to stack the counts of different pixels is that they do not differ in terms of for example resolution or spectral shape. As can be seen in fig. 4.5 this assumption is valid for this case as a clear spectrum was obtained for the summation of the counts. In addition, the Compton edge at 48.2 keV becomes observable in the summed spectrum. In the spectra of single channels, for example in fig. 4.1, this feature had a too weak signal to be identified. The highlighted region from 2 keV to 10 keV is the region of interest for the background index. Three quality cuts were applied to the data, without them the data cannot be stacked. Due to the application of the quality cuts, spectral peak M is no longer present as it is the pulser signal. It was removed along with the low-energy noise. Further information on quality cuts applied to the data is given in chapter section 5.2.

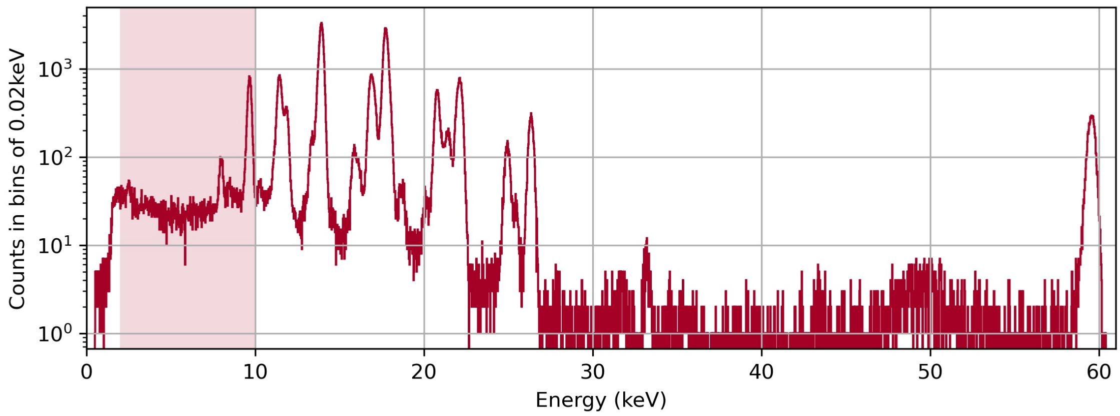

Figure 4.5: Stacked and calibrated ^{241}Am energy spectrum of all pixels. At an energy of 48.2 keV, the Compton edge corresponding to the 59.5 keV peak is visible. The red color band indicates the region of interest for the background index determination. All spectral peaks have a clear structure after the summation and the position of the spectral peaks agrees with the energy of the identified peaks in table 4.1. All three quality cuts (see chapter section 5.2) were applied, removing the pulser peak and the low-energy noise.

4.4 Fano limit and energy resolution

The Fano factor is based on radiation creating electron hole pairs in a material. In a purely Poissonian process the Fano factor is one [30]. For semiconductors the process is sub-Poissonian, which means that the electron-hole pair production is not independent but correlated, leading to a Fano factor smaller than one. The Fano limit is the minimal width of a peak, describing the statistical fluctuation of the production of charges [2]. Equation (4.2) can be used to calculate the Fano limit, by setting σ_{el} to zero.

$$\sigma_{Fano+Noise} = \sqrt{F \cdot w \cdot E + \sigma_{el}^2} \tag{4.2}$$

The curve has a square root shape with the FWHM increasing for higher energies (eq. (4.2)). Here, F describes a material dependent factor. For silicon (Si) a Fano factor of $F = 0.115$ is used for this thesis [27][31]. The factor w is another material dependent constant describing the energy that is necessary for creating an electron-hole pair, which takes the value of $w = 3.6$ for Si. The factor σ_{el} describes the electronic noise of the signal readout electronics, see eq. (4.3).

$$\sigma_{el} = \sqrt{\frac{FWHM_{59.5keV}^2}{8 \cdot \ln(2)} - F \cdot w \cdot E_0} \tag{4.3}$$

In this thesis we use the energy of the spectral peak at 59.5 keV for E_0. The energy resolution is calculated for the energy variable E. For a Gaussian peak eq. (4.4) gives the conversion between σ and the energy resolution value.

$$\sigma_{Fano+Noise} = \frac{FWHM}{2 \cdot \sqrt{2 \cdot \ln(2)}} \approx \frac{FWHM}{2.3548\ldots} \tag{4.4}$$

The Fano limit and the energy resolution curves for this setup for each channel can be found in fig. 4.6. Here, the energy resolution curve was extrapolated by using one data point only - the FWHM of the spectral peak Q at 59.5 keV. One point is insufficient to fit this energy resolution curve, especially when an uncertainty should be determined as well. However, the aim was to only retrieve a rough estimate for the Fano noise. Most pixels have an energy resolution of about 260 eV FWHM at an energy of 6.0 keV, only the energy resolution of channel 01 is worse with a value of 382 eV, due to an unknown reason. The energy value of 6.0 keV was chosen to better compare these resolution results to other calibration measurements, where mostly ^{55}Fe is used. ^{55}Fe has two prominent lines at 5.9 keV and 6.5 keV. The electronic noise of the channels is the value of the point where the respective lines cross the y-axis at 0 keV [2]. 10.0 keV is the upper limit of the energy range considered for the background index making it the energy with the largest FWHM values in the background index. A summary of energy resolution values for 0.0 keV, 6.0 keV, 10.0 keV and 59.5 keV of all channels can be found in table E.1.

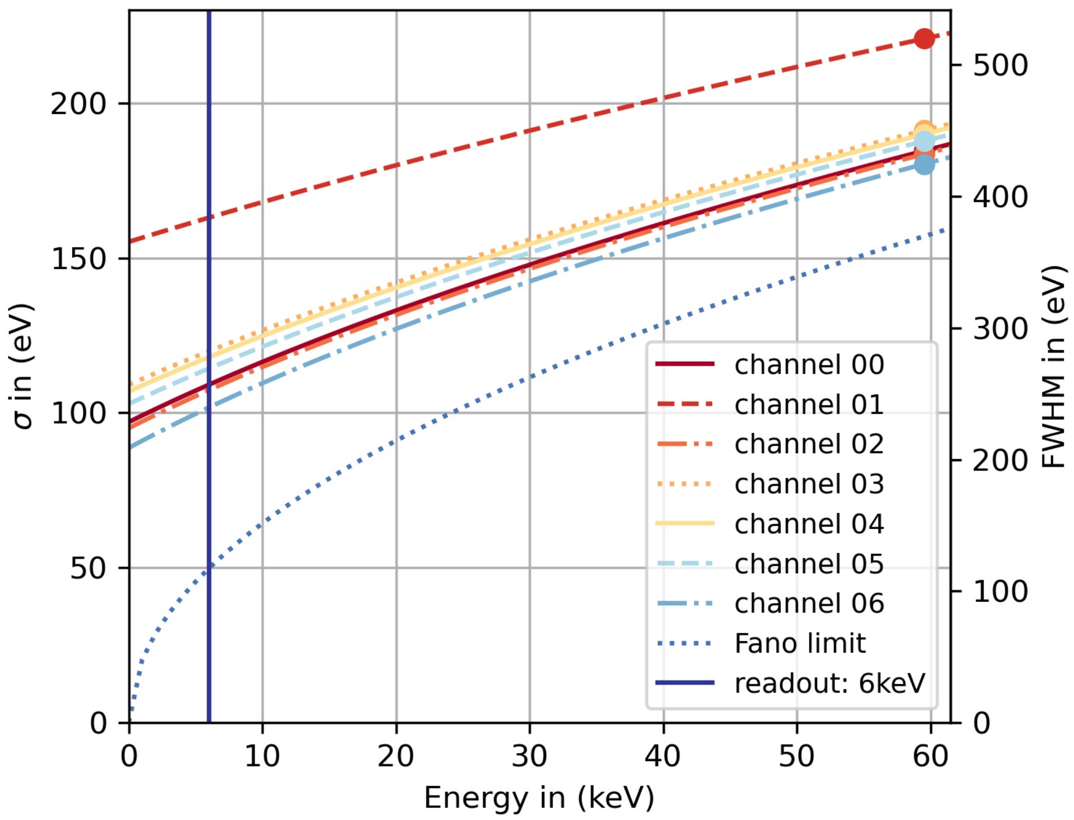

Figure 4.6: Energy resolution curves for the different detector channels. All pixels have a resolution of around 260 eV at 6.0 keV. Only pixel 1 features a worse resolution of about 382 eV.

The energy resolution at 6 keV in the detector geometry is shown in fig. 4.7. No obvious pattern is visible.

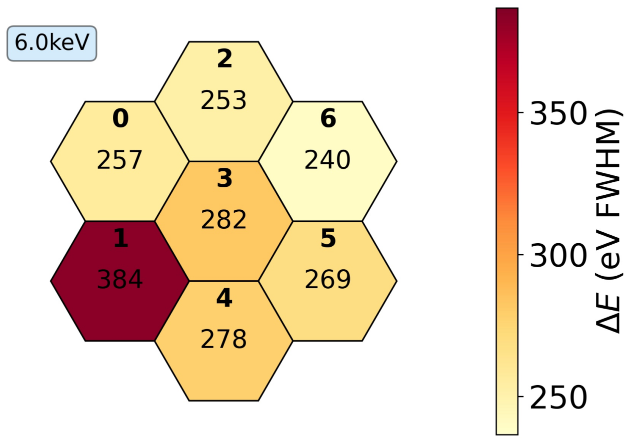

Figure 4.7: Energy resolution in eV of the different pixels at an energy of 6.0 keV. Pixel 1, on the lower left, shows a worse resolution than the other pixels.

5 Data Cleaning

The background of the TAXO demonstrator (described in section 3.4) was measured for 116 days. The data was recorded in 19 shorter measurements called runs. The runs run001 and run002 cannot be used as they belong to a different TAXO PCB. The calibration data is in run003, whereas run004 until run022 contain data of the background measurement.
Data acquisition does not only record signals which are useful and interesting. The irrelevant signals should be removed before the data analysis and this can be achieved by data cleaning. Besides the check for completeness of the recorded data, where each event should consist of eight waveforms, the event quality was taken into account as well. Therefore, characteristics of good pulse shapes were defined:

- flat and smooth baseline
- one trigger only
- exponential decay of the signal, of 14 ns, for all pulses

These criteria ensure that the energy reconstruction, described in section 3.3, returns correct values. In the following sections quality cuts, which ensure these criteria, are described. Examples of pulses, which fulfil the aforementioned criteria, are displayed in fig. 5.1.

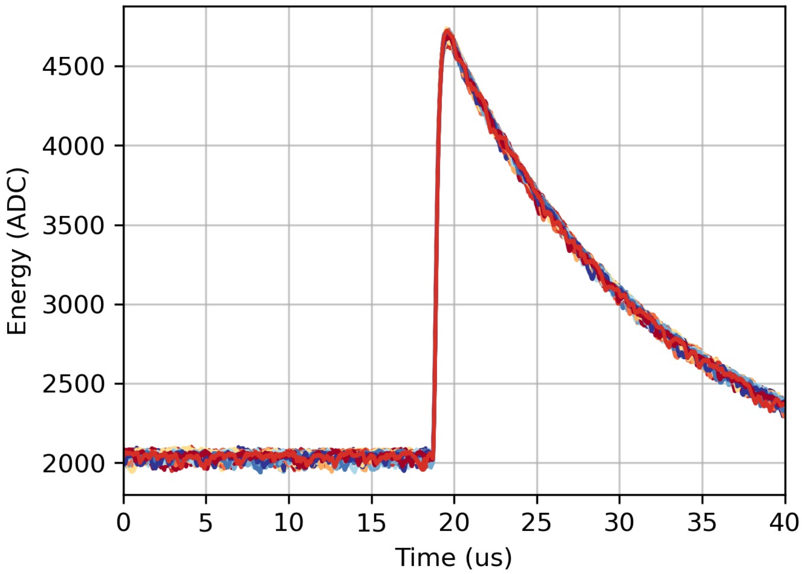

Figure 5.1: Example of 40 waveforms that satisfy the pulse characteristics, recorded with channel 01. The stable baseline, one rising edge and the same exponential decay rate are visible. The displayed pulses are pulser signals.

5.1 Stability of the recorded data

The measurement time of several months to gather sufficient data for the background index of the TAXO demonstrator in the deep underground laboratory at LSC ideally requires a stable data acquisition without drifts of any kind. All components of the setup, like the SDD, the readout electronics and the pulser, therefore need to have a stable operating mode. In the following section the stability of the pulser and the baseline properties of the waveform are described.

5.1.1 Pulser stability

The pulser is used to monitor the function of the bias system. A prerequisite for using the pulser as a monitoring device is to check first whether the pulser was stable itself. The pulser remained stable throughout the entire measurement, which is visualised in fig. 5.2, apart from three small instabilites in run005, run010 and run020 and a slight decrease. A similar pattern can be seen in the baseline value (see section 5.1.2). This drift of the pulser towards a lower energy (< 0.5 ADC) is much smaller than the spread of 3 ADC. The calculated drift in energy obtained by fitting the data with a linear function was −0.012 % compared to the starting value. Figure 5.2 displays the pulser over the background run time. The linear fit of the pulser signal (solid pink line) and the pulser position in the beginning (dashed blue line) almost overlap. This means that any significant instability in the SDD pulser events indicates changes in the detector gain, rather than a change of the pulser amplitude itself.

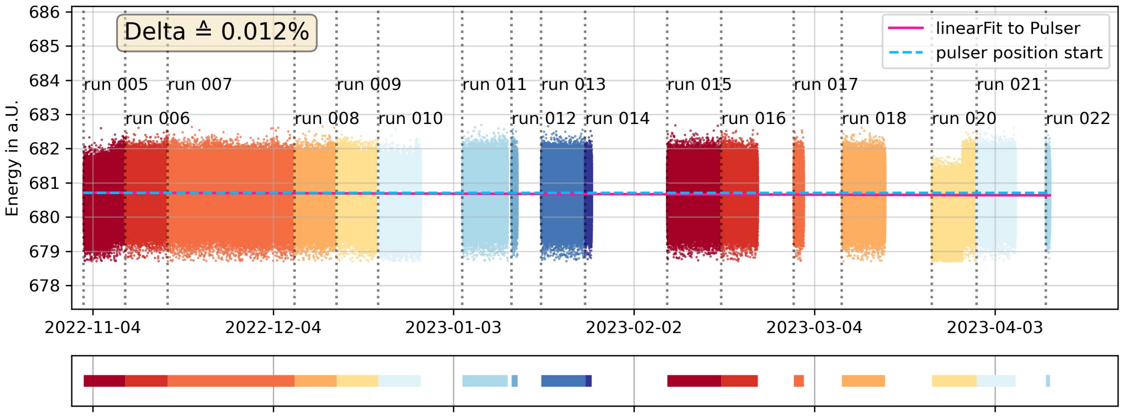

Figure 5.2: Pulser position over time for the background data acquisition. The recorded negative drift of −0.012 % over the entire measurement time is small. This can be seen by the comparison of the linear fit of the pulser (solid line) and its original position (dashed line) in the beginning.

The pulser signal is recorded by all seven pixels of the SDD. Figure 5.3 displays the pulser signal recorded by channel 02 over the whole runtime. The pulser signal drifts downwards by −0.6 % starting from the run005 to run022. The absolute drift is −0.1432 keV. In addition, there is a difference between the starting position of the pulser in run003 (not in the figure) and the average position at the beginning of run005. This offset was not further investigated.

Figure 5.4 summarises the drift of the pulser in percent for all channels of the detector and for the pulser itself. The drift values in percent as well as in keV can be found in table F.1.

A drift is present in all channels, except in the pulser channel. This implies a change in the detector gain, which could be explained by a decreasing voltage in the power supply of the detector chip. The difference between the channels can be explained with slightly different readout electronics for each channel. As the pulser provided signals of constant energy, the channels recorded a decreasing energy. This means

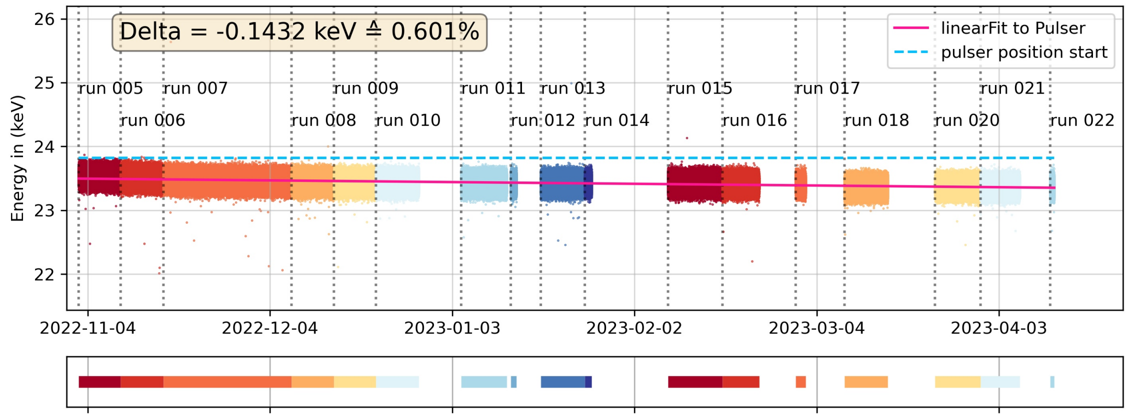

Figure 5.3: Example pulser data from the background measurement (channel 02). The starting position of the pulser from run003 (dashed blue) shows a shift with regard to run005. The linear fit of the pulser signal (solid pink line) shows a negative drift from run005 to run022 with a decrease of the energy by $-0.6\,\%$.

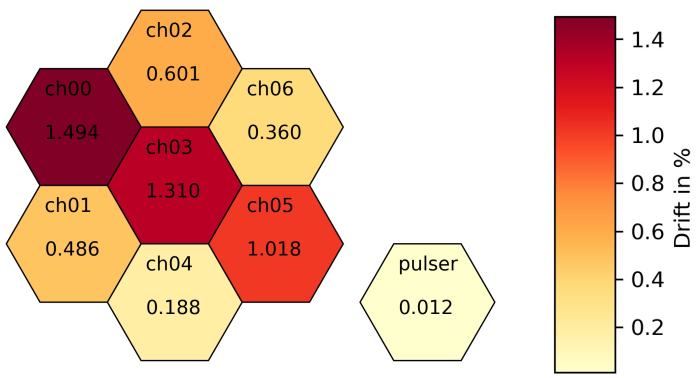

Figure 5.4: Negative drift of the pulser over the measurement time in % for all detector channels and the pulser channel. The detector pixels with the largest energy drift are aligned in an axis from the top left to the bottom right. The reason for this structure is not clear, but could be due to electronic readout dependencies.

that the energy seen by the channels has a bias to lower values. The energy drift can be corrected in the offline processing. The resulting bias for a channel is at most the respective energy resolution. An exact energy reconstruction was not in the scope of this thesis, therefore, the decision was taken not to correct the energy values.

5.1.2 Baseline stability

A stable baseline over the course of the entire measurement time is desirable. A drift can indicate a changed leakage current, which could stem for example from temperature changes. Figure 5.5 displays the absolute baseline value exemplary for channel 02 for run005 to run022 before the application of quality cuts. The baseline is constant apart from some minor dips in run005, run010 and run020. In addition, for the selected time range a small amount of baseline values are lower than the majority. The distribution is not equal in both directions, as there are very few baseline values lying above the main band.

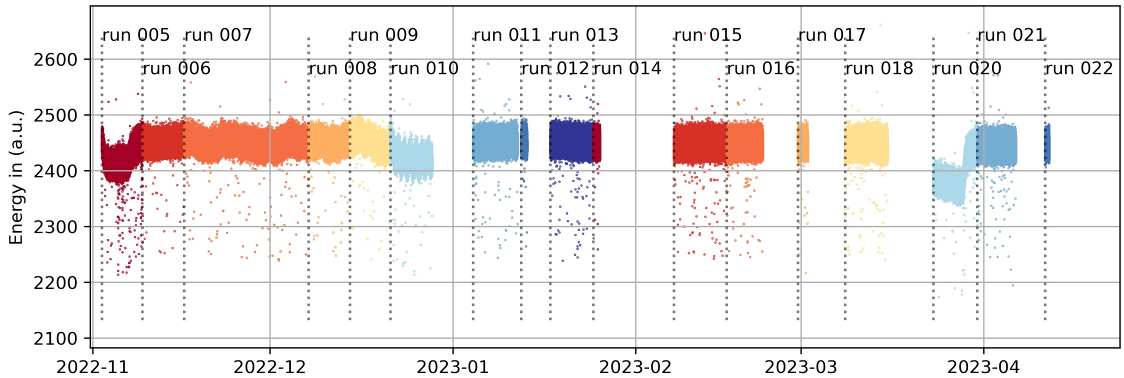

Figure 5.5: Absolute baseline value of channel 02. It is stable, except for minor dips in run005, run010 and run020. Several more baseline values appear underneath rather than above the band.

5.2 Quality cuts

A detailed study of the measured background data revealed that the data collection contained waveforms which were not usable for the analysis of the background. There was an issue with the recording itself, where signal waveforms were not recorded for some timestamps for individual channels. The offline processing exposed multiple triggers in waveforms and incorrect energy reconstruction due to waveforms with sloping baselines. This motivated the use of quality cuts to remove incomplete and incorrectly reconstructed events.

5.2.1 Timestamp mismatch - first quality cut

Each event is supposed to consist of eight signals recorded at the same time: seven waveforms from the respective pixels of the SDD and one waveform from the pulser. For most runs the data recording missed one or more channels for varying amounts of time, misaligning the data. In order to reconstruct an event the timestamps need to be compared. The reason for this DAQ malfunction is not clear yet, but it will be studied in the future to improve upcoming measurements.

Figure 5.6 shows the recorded timestamps for three different runs for each of the eight channels. Figure 5.6a displays an example of a complete dataset, where each event has a complete set of recorded channels. This dataset represents the ideal case. Most of the background runs featured a loss of records of varying degree. A medium case of dataloss can be seen in fig. 5.6b, where the missing records appear as thin white lines. A severe case of dataloss is displayed in fig. 5.6c, where the first two thirds of the dataset have large gaps. In the last third of the dataset only one channel was recorded for each time point. In addition, the respective timestamps corresponded to a date which did not agree with the actual time period of the run. This error feature only occurred in two runs - run004 and run019. The cause of this error was not further investigated.

The background measurement consists of 19 runs. Run019 had complete records for only 55% of all recorded timestamps. The other eighteen runs had complete events for more than 90% of the recorded timestamps. Out of those, eight runs had almost only complete events. Figure F.1 shows the usable amount of data for each run.

As only complete records of events are usable, all incomplete events were removed from the analysis. The completeness check of an event is the first quality cut - *QC1*.

5.2.2 Multiple triggers and a sloping baseline - second quality cut

The signal processing, described in section 3.3, is designed for typical SDD waveforms, without additional features. These events have at most one pulse per channel and each pulse has a single trigger, a flat baseline and a regular decay, which looks like the pulses in fig. 5.1. For each identified trigger an amplitude is calculated. Noise

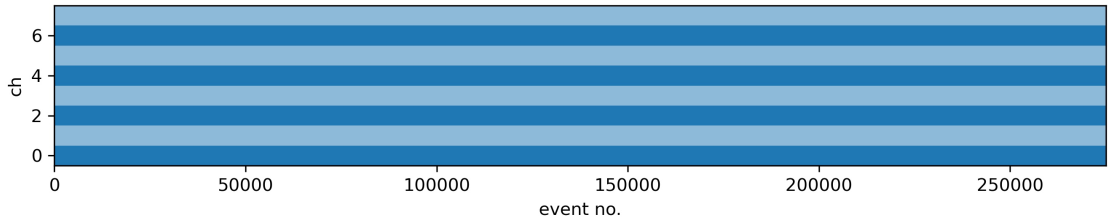

(a) complete dataset - each event has a complete set of recorded channels (run006).

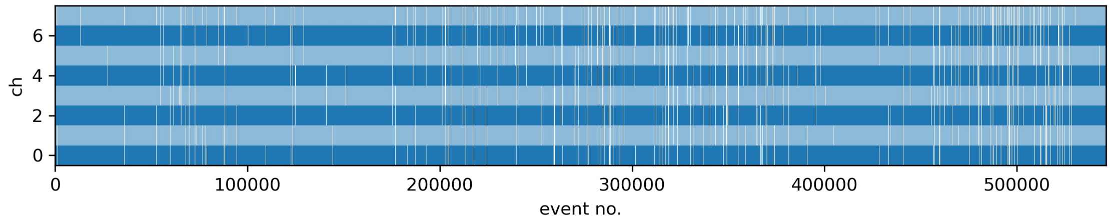

(b) incomplete dataset - some events lack one or more channels, visible as white lines (run013).

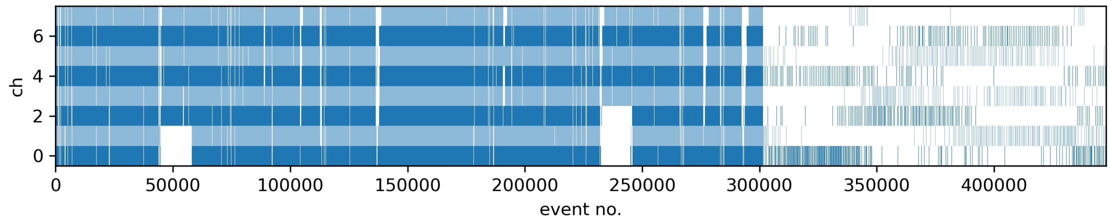

(c) incomplete dataset - significantly more events lack the information of one or more channels. In addition, the last third of the run features an entirely different type of data loss, as precisely only one channel was recorded for a given timestamp. These timestamps carry an additional error, where they are assigned to a future time, not related to the actual time span of the run.

Figure 5.6: Timestamp mismatch of varying degree - (a) no data loss, (b) medium data loss and (c) significant data loss

bursts, reset signals or in-trace pileup can fulfil the trigger criterion, too. Sloped baselines, caused by pre-trace pileup (downward slope) or reset trigger tails (upward slope), impact the reconstructed amplitude value as well.

A second quality cut (*QC2*) was introduced, in order to remove unsuitable events and thereby ensure accurate energy determination. QC2 takes into account the number of triggers as well as the slope of the baseline.

5.2.2.1 Trigger count

A pulse can be identified by a rising edge which passes a threshold. Proper pulses feature only one trigger, ideally in the middle of the recorded time window. Pileup events have more than one trigger. Noise bursts as well as reset signals have rising edges, too, which are recognised by the trigger filter as well. An amplitude value is calculated for each trigger position. Neither the amplitudes for noise bursts and reset signals nor amplitudes of pulses with at least one of these features can be used. The applied amplitude calculation only works for proper pulses described at the beginning of this chapter. Details on the amplitude calculation can be found in section 3.3. In order to remove events with distorted pulse shapes from further analysis, each event with more than one trigger gets a flag.

Figure 5.7 displays waveforms where more than one trigger was present. Most of these waveforms have a reset signal in the second half of the time window.

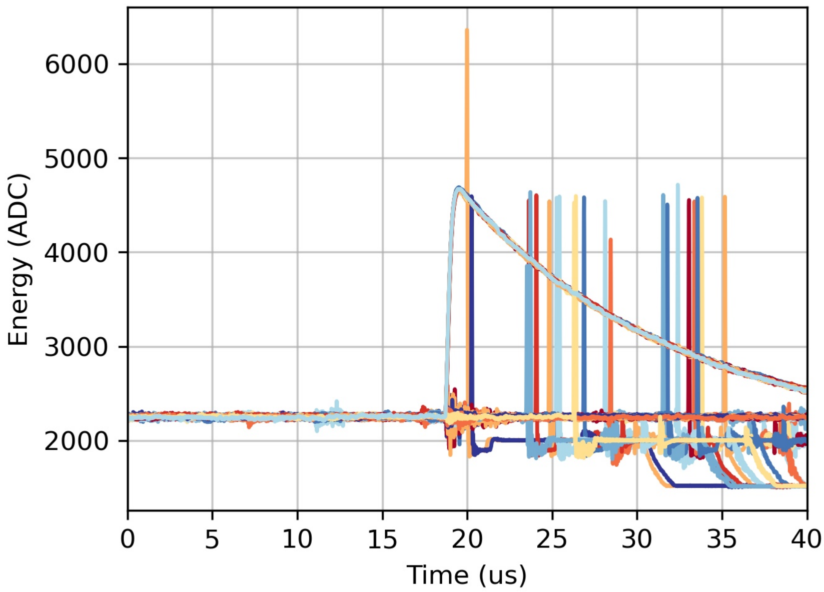

Figure 5.7: QC2 - example of 60 waveforms of the background spectrum, recorded with channel 03, which feature more than one trigger. Most of them contain a reset signal in their second half.

5.2.2.2 Sloping baselines

Another feature which can lead to wrong energy reconstruction by applying a trapezoidal filter are sloping baselines. Figure 5.8 shows some example waveforms with upward sloping baselines. Upward sloping baselines are most probably caused by a preceding reset signal. Downward sloping baselines, not present in the figure, can be explained by a so called pre-trace pileup. The downwards sloping baseline is the tail of a preceding pulse.
For the energy reconstruction the average position of the baseline of a waveform is used as its zero. Events with an upward sloping baseline are assigned a higher energy, as the average lies below the regular baseline position. The height of the pulse remains the same, leading to a higher reconstructed energy. A downward sloping baseline faces a higher zero position compared to the regular case and thus is assigned a lower energy.

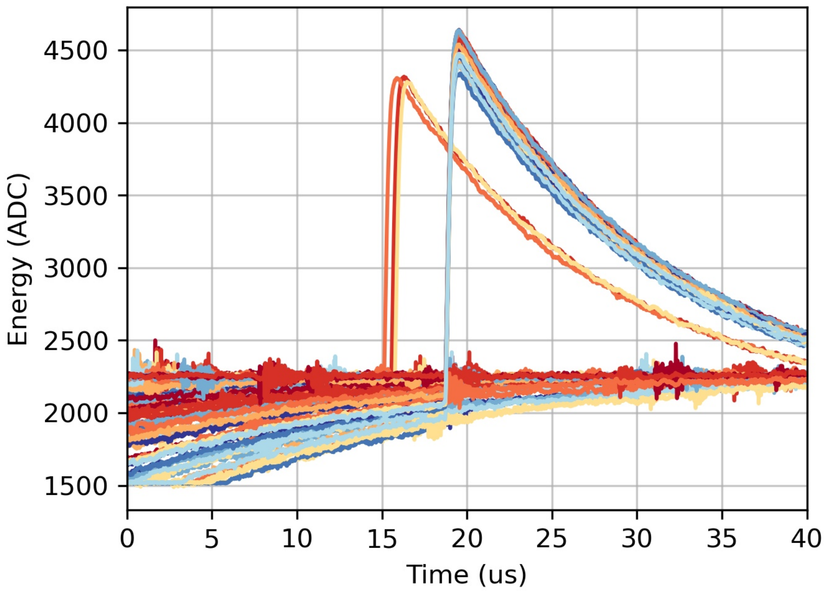

Figure 5.8: QC2 - example of 60 waveforms which feature a sloping baseline. The magnitude of the slope varies among the displayed waveforms.

5.2.2.3 Baseline variation

The baseline variation is determined by calculating the standard deviation of the ADC values for the time that the baseline was recorded. The baseline variation values

of the background data (run004 up to including run022) can be seen in fig. 5.9. Each channel has a clear peak with small baseline sigma spread where the bulk of the counts is situated and a tail towards higher values. Channel 01 has a significantly broader peak which additionally is shifted to the right, indicating worse noise performance. The shape of the tail varies as well for the different channels. Channels 01, 03, 04 and 05 have a flat distribution for high values of energy spread, while channel 02 and 06 show a decline. Channel 00 features comparably high count rates for the high baseline sigma values. The reason for this behaviour was not further studied.
Baseline variations can be caused by electronic noise of the setup. Another source of large spread are sloping baselines caused by earlier events. Both features have an impact on the energy reconstruction process. Therefore, all waveforms with a baseline variation value of more than 20 were removed. For channel 01 this limit was set to 40.

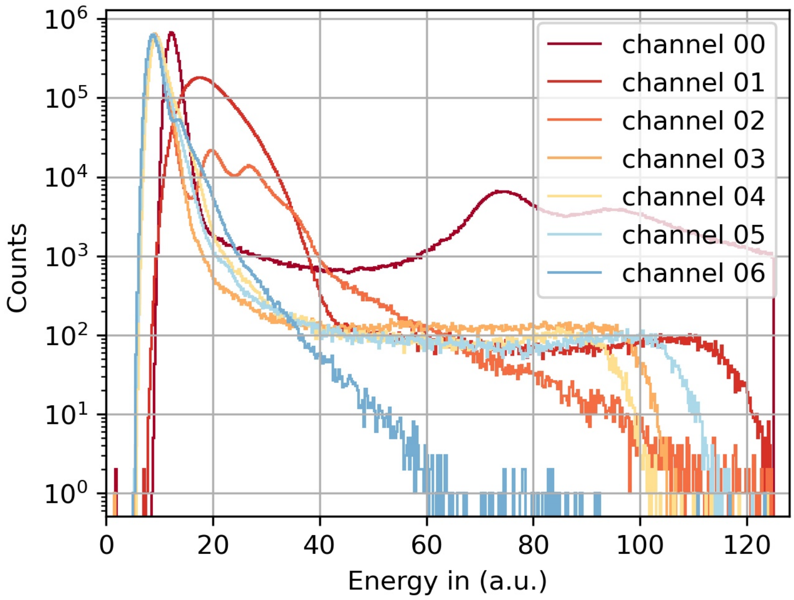

Figure 5.9: Baseline sigma values of the entire background measurement (run004 up to including run022) for all channels. Each channel has a dominant peak below 20 ADC. The peak of channel 01 is significantly broader than the peaks of the other channels. In the region of high baseline variations channel 01, 03, 04 and 05 feature a flat tail, whereas channel 06 has almost no tail. Channel 00 and 02 have additional peaks.

5.2.2.4 Effect of the baseline cut

Figure 5.10 displays the reconstructed pulser signal energy (channel 03) before and after the second quality cut, which removes events with sloping baselines and multiple triggers. The pulser band before the cut, displayed in the top plot of fig. 5.10, consists of a main band with a tail shifted to higher energies, which has a lower density of points. The bottom plot of fig. 5.10 displays the pulser data after the cut. The tail, on top of the main band, was removed. Events in the tail had an upward sloping baseline, which fits to a higher reconstructed energy. To illustrate the effect of QC2, an example of waveforms from the main band and the tail are displayed in fig. 5.11a and fig. 5.11b respectively.

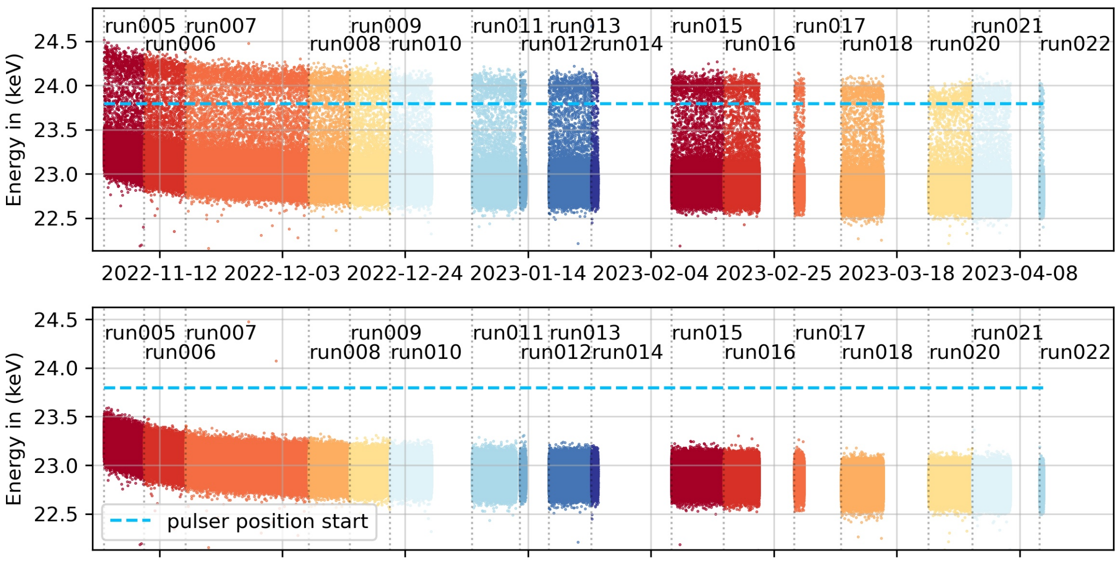

Figure 5.10: Pulser signal of the background measurement (recorded by channel 03). The top figure is the dataset before QC2. The figure on the bottom displays the dataset after removing all events which have either a sloping baseline or multiple triggers or both. The tail is removed with QC2, leaving a well defined band of the pulser signal for the whole dataset.

In fig. 5.12 a more detailed inspection of the baseline parameters is given. The displayed data stems from the main band and its tail of run006 recorded by channel 03. The data points were assigned to the main band and tail by the absolute energy of the pulse. The assumption that events in the tail feature high sigma values of the baseline is verified in fig. 5.12a. The previously described cut for $\sigma > 20$ for channel 03 is therefore valid. This cut effectively removes sloped baselines. A similar

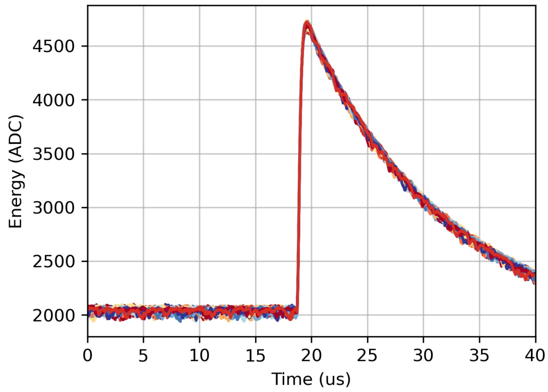

(a) waveforms from the pulser band, with a stable baseline.

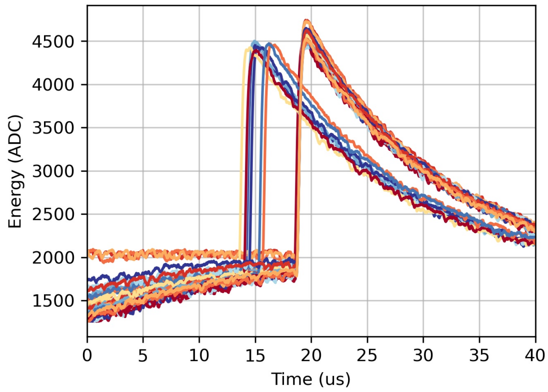

(b) waveforms from the tail, with clearly visible sloped baselines. Some waveforms have an earlier trigger, this effect was not further studied.

Figure 5.11: Waveform examples for the two different pulser band regions.

effect can be seen for the absolute baseline value in 5.12b. Here the low values correspond to events in the tail. In principle, a cut could have been applied to the the absolute baseline values instead of the standard deviation. The advantage of using the variation of the baseline as a quality criteria is that the cut can be applied to all channels and runs. The absolute baseline value on the other hand can vary for channels and runs. An unstable baseline can hint at additional noise in the waveform. The general applicability and the sensitivity to noise make the sigma value of the baseline a better candidate for a quality cut.
Another tested hypothesis was the connection between trigger number and events in the tail. Figure 5.12c shows the distribution of the trigger number for all of the selected events, the main band and the tail. According to this figure, events in the tail have one trigger only. Therefore, the trigger number cannot be effectively used as a quality cut to reject events from the pulser tail.

The evolution of the baseline sigma values for the entire measurement time without quality cuts is shown in fig. 5.13, exemplary for channel 02. With run011 the spread in the baseline value has a fourfold increase. In addition, there are two runs with a change of the baseline values. The investigation of the changing baseline sigma value was beyond the scope of this thesis.

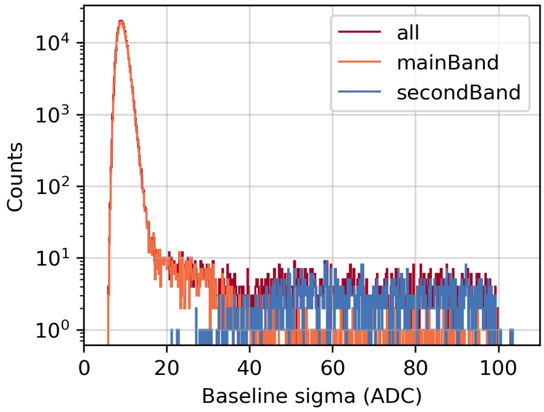

(a) Baseline sigma value - main and second band separated.

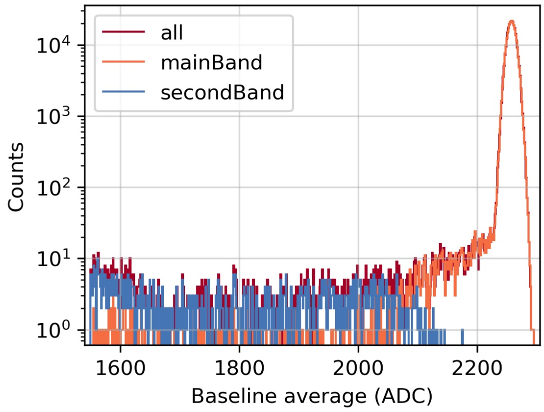

(b) Baseline absolute value - main and second band separated.

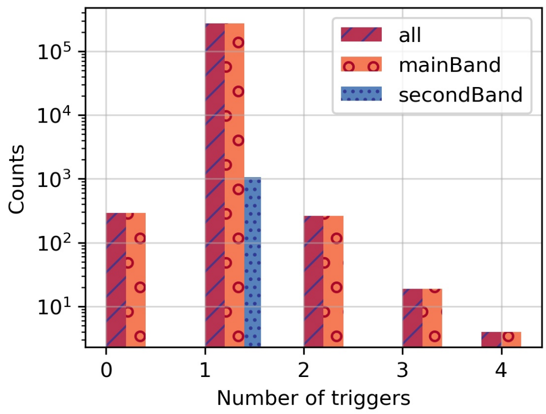

(c) Baseline trigger number.

Figure 5.12: Baseline characteristics - baseline variation, absolute baseline value and trigger number

5.2.3 Pulser identification and multiplicity definition - third quality cut

To determine the background index, it is necessary to only include events that are actual signals. The third quality cut (QC3) therefore removes the pulser signal and noise signal, present at low-energy, from the background data.

The pulser signals are visible in all channels. If channel 07, which exclusively records the pulser, has a signal, the event is marked as a pulser event. Events of channels 00 to 06, which happen at the same time a pulser event is registered, are excluded from the background analysis.

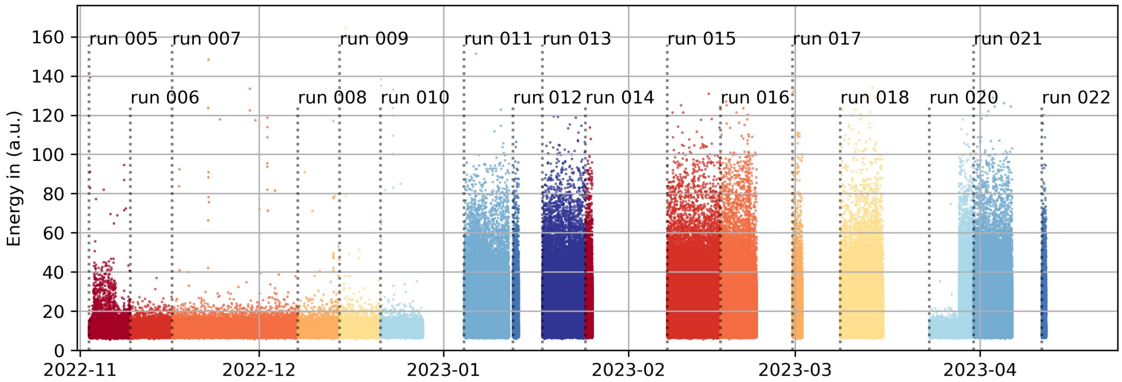

Figure 5.13: Baseline sigma values for the entire background measurement without quality cuts. There are two stable periods. The first starts with run006 until including run010, and the second for run011 until including run022. Between the two groups there is roughly a four fold increase. Run005 and run020 have a change of the sigma value during their respective runtime, this effect was not further investigated.

The event energy is a sum of the energies recorded by all channels. Thereby, the energy of charge sharing events is properly accounted for. Charge sharing happens when the charge cloud is created between pixels such that two or even three pixels record parts of the energy. Summing over all energies would include noise signals, which happen simultaneously in other pixels, but have no connection to the actual event. In order to identify charge sharing and noise, each pulse with a reconstructed energy of more than 0.5 keV is assigned a multiplicity flag. These flags are summed for each event. Events of multiplicity zero, which potentially contain low-energy noise, were removed from the dataset.

Events remaining after the third quality cut have a recording of all channels, a proper energy reconstruction, are not caused by the pulser and are not part of the noise.

5.3 Effect of the quality cuts

The three quality cuts, described in section 5.2, are applied to the data subsequently. The result is a cleaned dataset with events that have a recording of all eight channels and an accurate energy reconstruction, and which are neither a pulser signal nor noise. This cleaned dataset can be further analysed.

5.3.1 Calibration run

To calibrate the energy of the TAXO SDD demonstrator a measurement with ^{241}Am was performed - see chapter 4. In fig. 5.14 the event energies of the calibration data can be seen. To obtain the event energies, calibration functions were applied to the data of the calibration run. Then the three quality cuts, described in section 5.2, were applied. The difference between the obtained spectrum and fig. 4.1, which displays the uncut data, are the removed noise signals close to 0 keV as well as the removed pulser signal. The features of the ^{241}Am spectrum are clearly present. Among them, the photon peak at 59.5 keV is visible along with its Compton edge at 48.2 keV.

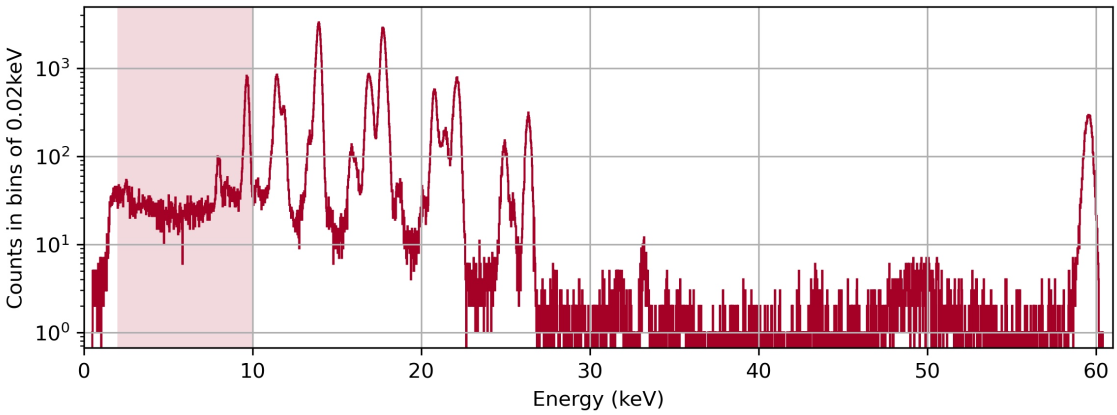

Figure 5.14: ^{241}Am spectrum - calibrated and summed over all channels after application of the three cuts.

Figure 5.15 shows in addition the multiplicity distribution of the calibration data. The signal consists mainly of events of multiplicity one. In regions of higher count rates, for example between 10 keV to 30 keV as well as around 59 keV, events of multiplicity two and even three can be seen.

5.3.2 Background run

To see the effect of the three quality cuts on the background data, run007 was picked as an example. The full spectrum is displayed in fig. 5.16. Only a few events remain after the quality cuts. The highlighted region is the region of interest for this thesis. Only counts between 2 keV to 10 keV will contribute to the background index calculated in section 6.1.

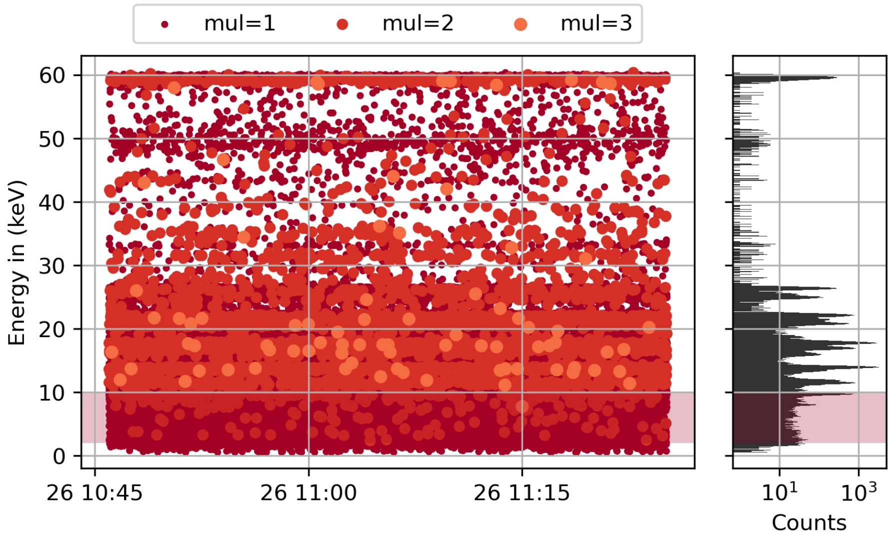

Figure 5.15: Multiplicity of the calibration run (run003) (left side) and its summed spectrum (right side) - after application of the three quality cuts.

The multiplicity distribution of the background data is shown in fig. 5.17. The events have mainly multiplicity one, the remaining have a multiplicity of two.

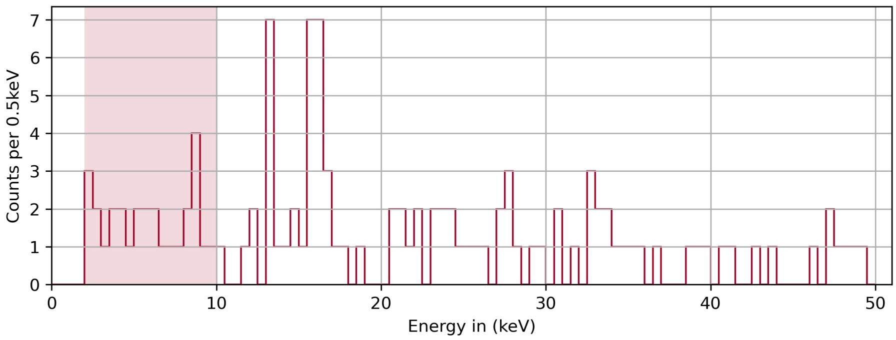

Figure 5.16: Background spectrum of run007 after application of the three quality cuts and summation over all channels. The region of interest is given by the shaded red area.

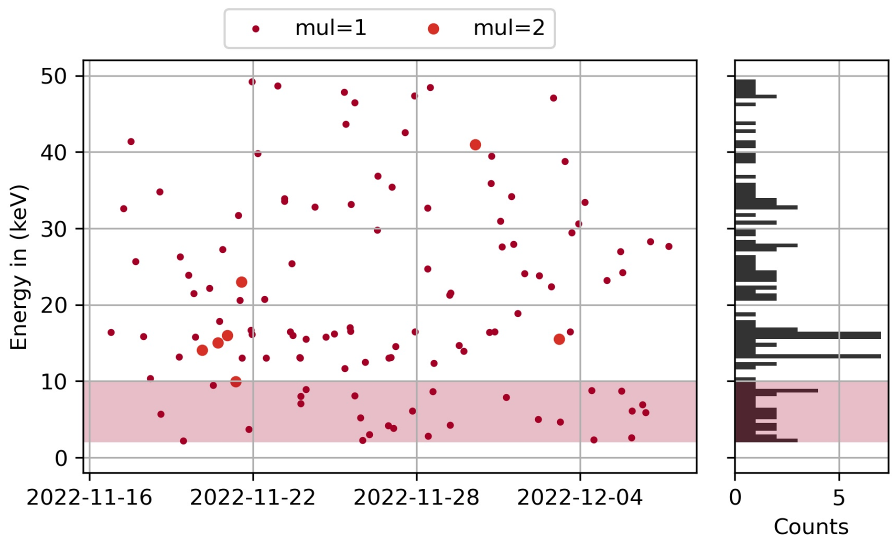

Figure 5.17: Multiplicity distribution of run007 after application of the three quality cuts and summation over all channels. Only few events with multiplicity two are present.

6 Background index

To determine the background of the TAXO SDD demonstrator and the signal readout electronics, a dedicated long-term measurement (116 days) was performed in the underground laboratory Laboratorio Subterráneo Canfranc (LSC) in Canfranc. After identifying and rejecting unsuitable events within the entire background data set, based on several quality criteria (see section 5.2), the background index can be calculated with eq. (6.1).

$$I_{background} = \frac{c}{\Delta E \cdot T \cdot A} \tag{6.1}$$

The background index $I_{background}$ is defined as the number of background events c observed in a given energy window ΔE (here 2 keV to 10 keV), for a time period T by a detector of area A. The determination of the event energy is described in section 3.3. The active area of the seven pixel TRISTAN SDD detector are 0.41 cm^2 (see chapter 3).
To retrieve the duration of the data acquisition for the background index calculation the pulser signal is used. The pulser signal contains information on the real active time of the setup. The pulser rate was set to 0.5 Hz. The pulser GUI of the setup provided a monitoring system which showed the elapsed time and the number of pulser events. From this data an actual frequency of 0.46 Hz was determined, which is used in the following analyses. The reason for this deviation was not further studied. Downtimes of the setup are caused by the reset pulses. The pulse generator has been programmed such that the time distribution of the events follows a Poissonian distribution. This was done to ensure that the pulser signal does not coincide with the reset pulse for extended periods of time. The idea is that the pulser events will coincide with the reset signal for the same fraction of time as real background events.

Starting with the total background measurement time, first *QC1* is applied, where part of the data is rejected due to incomplete event recordings (see section 5.2.1). Secondly, *QC2* ensures that events featuring multiple triggers or a noisy baseline, are removed. The number of pulser events which pass both quality cuts *QC1* and

QC2 is divided by the pulser rate (0.46 Hz) to obtain the active measurement time in seconds.

Another value which can be attained from the pulser is its acceptance rate. The acceptance rate is the fraction of pulser signals which passed *QC2* divided by the number of pulser events passing *QC1*. The lower the acceptance rate, the longer a measurement will take to collect the same amount of useful data. The acceptance rate for this background measurement ranges from 98.08 % to 98.61 % for each run (compare with fig. 6.1). This is an acceptable value, as the reset was expected to have a small influence on the active measurement time.

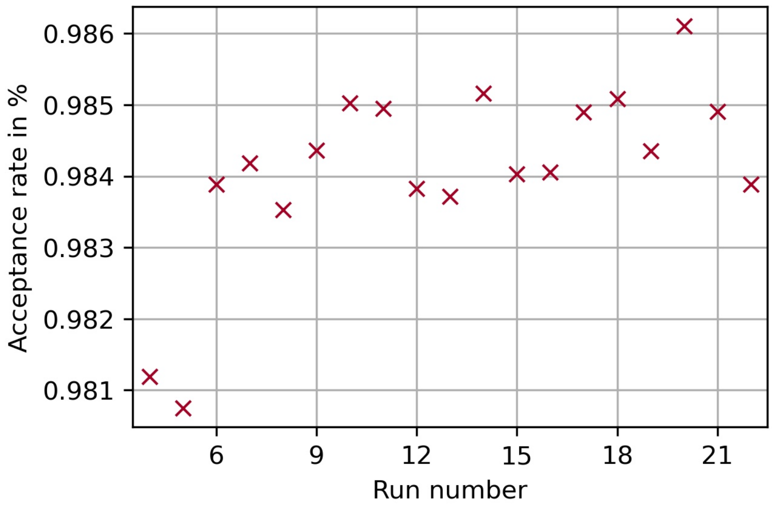

Figure 6.1: The acceptance ratio of the pulser is the number of pulser events after QC2 divided by the number of pulser events after QC1. The ratio indicates how much of the dataset is usable after removing events impacted by reset triggers, pileups and excessive noise. The acceptance rate lies between 98.08 % to 98.61 %.

6.1 Background index result

With all the necessary inputs present, the background index was calculated. Figure 6.2 shows the calculated background index for each run with uncertainties using the method by Feldman and Cousins [32]. The background index was calculated for each run separately. Most runs have a background index in the range between 0.4×10^{-5} counts/keV/s/cm^2 to 0.8×10^{-5} counts/keV/s/cm^2. Two runs (run011 and run014) did not record any events in the region of interest. Run022 has the largest uncertainties which can be related to its short measurement time. The background index values for run004 until run010 fluctuate less than for run011 onwards. There was a power outage in the laboratory room, causing a shutdown of our measurement setup after run010, which could have had an impact on the later measurements.

To determine the final background index, all collected counts between 2 keV to 10 keV for all channels were summed and divided by the total active runtime, the area of the detector and the selected energy range. The final background index including all runs is $(5.9 \pm 0.5) \times 10^{-6}$ counts/keV/s/cm^2.

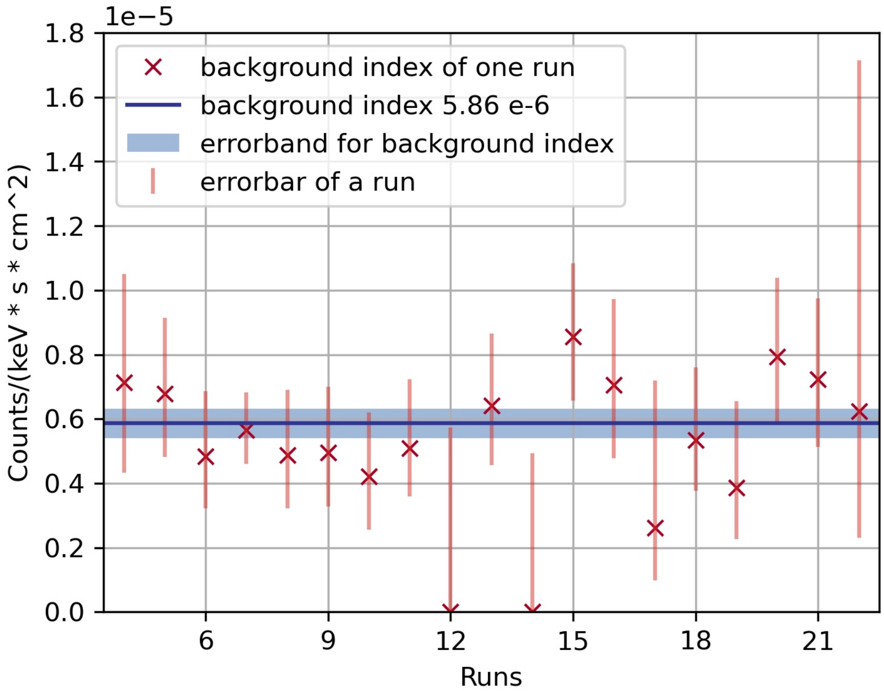

Figure 6.2: Calculated background index for the TAXO SDD demonstrator setup at the LSC underground laboratory. The active measurement time was 116 days. The total background index has been calculated by determining the background index of each run and taking an average. In most runs, a background index between 0.4×10^{-5} counts/keV/s/cm^2 to 0.8×10^{-5} counts/keV/s/cm^2 was obtained, no events were recorded for run011 and run014.

The summed background spectrum index for all runs as well as a simulated energy spectrum for the TAXO SDD demonstrator is displayed in fig. 6.3. The simulation data in fig. 6.3 was provided by C.Wiesinger [28]. The recorded background spectrum features a low count rate of 165 counts in the region of interest over 116 days. As a consequence, the statistical uncertainty is large. This has to be taken into account when comparing the measured background spectrum index with the simulation.

The measured background spectrum index features multiple peaks. In general, the position of the features is in agreement with the simulation. This agrees with the assumption that the energy calibration together with the bias voltages stayed constant over the entire measurement time of several months. A shift between the simulated and measured spectrum would hint at changed calibration values.

When comparing the measured background spectrum with the simulated one in more detail, small differences can be observed.
Both spectra have peaks at 13.0 keV, 15.3 keV and 16.3 keV. Those can be attributed to X-ray lines from ^{238}U and ^{232}Th decay chains. These lines should be only visible when the respective isotope is located in close proximity to the SDD. They could for example stem from the PCB material that is used for mounting and connecting the detector chip. In particular, an origin from a farther source can be excluded since the X-rays would have been absorbed by the shield made of Cu and Si [27].
Regarding the differences between the measured and the simulated spectrum the following observations can be made: One prominent peak at 8.0 keV, an X-ray fluorescence of Cu, and another peak at 10.8 keV, which could stem from ^{210}Pb or ^{232}Th, are missing in the background measurement. This might be caused by differences between the actual setup and the simulation implementation. The copper fluorescence line, originating from the copper shield, could have been absorbed by the silicon plate, which in reality sits closer to the SDD than implemented in the simulation. The second missing line could be due to an irregular distribution of the impurities in the PCB. If they are located in a deeper layer of the PCB board lower energy lines could get absorbed by the PCB itself.

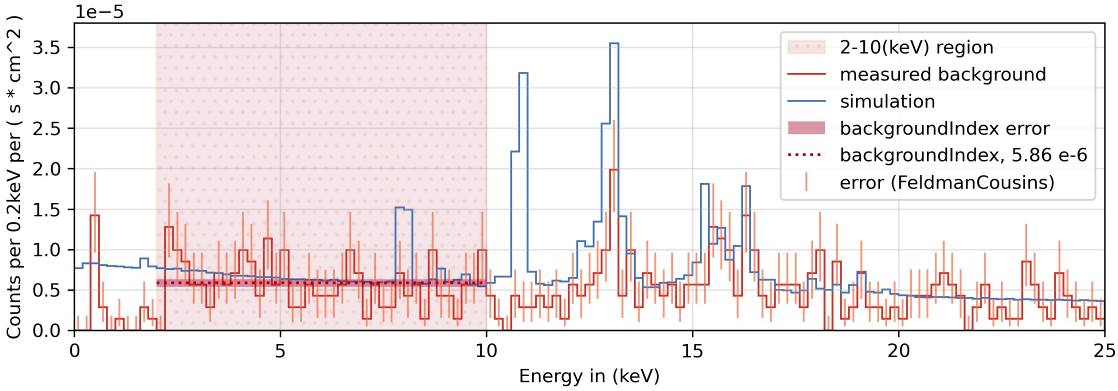

Figure 6.3: Background spectrum index in bins of 0.2 keV (in red) with errorbars (vertical orange lines). The average value of $(5.9 \pm 0.5) \times 10^{-6}$ counts/keV/s/cm^2 is depicted by a horizontal red dotted line. The measured spectrum agrees with the spectrum of the simulation (blue line). The red-dotted color band indicates the region of interest (2 keV to 10 keV) for the calculation of the background index.

6.2 Result discussion

The goal of the BabyIAXO experiment to be able to explore new parameter space of the proposed axion particle, requires a detector with a background index below 10^{-7} counts/keV/s/cm^2 [11], or equally 3 counts/keV/year/cm^2 (see section 2.2). The count rate of $(5.9{\pm}0.5){\times}10^{-6}$ counts/keV/s/cm^2, or equally about 200 counts/keV/year/cm^2, measured with the current TAXO SDD demonstrator is more than one order of magnitude higher. However, upgrade plans are in place to improve the background further towards the BabyIAXO goal.

It is assumed that the increased background level measured with the TAXO SDD demonstrator setup can be related to the detector PCB material. A radiopurity assay of the PCB material showed that it was not as clean as initially assumed [27]. Exchanging the material will reduce the background. The planned upgrade of the TAXO SDD setup will use PCB boards consisting of two pieces. There the PCB is cut at the neck, separating the head from the body (see fig. 3.5). Here, the head and neck of the PCB is made of silicon, whereas the body of the PCB will be made of a different PCB material, which has better radiopurity values than the one used for the PCB from this background measurement.

7 Conclusion

In this thesis the background index of a seven pixel TRISTAN SDD in a dedicated setup was determined from a 116 days long measurement located in the deep underground laboratory LSC. First a short energy calibration measurement was performed using an ^{241}Am source. The spectral peaks of the ^{241}Am data were selected and identified. For each pixel of the TRISTAN SDD a precise calibration was obtained. To improve the peak identification step in future measurements a longer acquisition time would be beneficial. After the energy calibration measurement, background data was acquired with the same setup.

The collected data consists of events which are composed of waveforms of all seven pixels as well as the waveform of the pulser. Collected events featuring reset pulses or pileup events are not of interest. Therefore, a data cleaning step was introduced to remove these parts of the data.

The signals generated by the pulser were used to monitor the measurement over the whole time period. With their help the stability of the gain was shown, as well as the live time of all pixels over the entire measurement.

The background index determined for the TRISTAN SDD in the aforementioned setup is $(5.9 \pm 0.5) \times 10^{-6}$ counts/keV/s/cm^2. The required value for the BabyIAXO experiment is less than 10^{-7} cts/keV/s/cm^2. The background in the current setup is hence more than one order of magnitude higher than the desired value. With the obtained spectrum a hypothesis for the exceeding background was established. The printed circuit board (PCB) containing the TRISTAN SDD possibly contains more radio-impurities than expected. This is supported by comparing the measured spectrum with a simulated one and confirmed by radio assay measurements of the PCB material. In order to test this hypothesis an upgrade of the setup, which was used for this thesis, is planned. The upgraded version will have an updated PCB design, and will be made of a more radiopure material. These measures are expected to reduce the background index in the future.

8 Bibliography

[1] (2020) LEITFADEN ZUR ERSTELLUNG WISSENSCHAFTLICHER ARBEITEN AM LEHRSTUHL FÜR UNTERNEHMESFÜHRUNG. [Online]. Available: https://www.fa.mgt.tum.de/fileadmin/w00chf/cm/03_Studium_und_Lehre/03_Abschlussarbeiten/210817___Leitfaden-Zur_Erstellung_Wissenschaftlicher_Abschlussarbeiten_Lehrstuhlspezifisch.pdf

[2] D. Spreng, “Energy Calibration of the TRISTAN Silicon Drift Detectors,” Bachelor’s Thesis, Technical University of Munich, October 2020.

[3] “Planck reveals an almost perfect Universe,” 2013. [Online]. Available: https://www.esa.int/ESA_Multimedia/Images/2013/03/Planck_cosmic_recipe

[4] “Dark matter.” [Online]. Available: https://home.cern/science/physics/dark-matter

[5] D. Perkins, *Particle Astrophysics*, 2nd ed., ser. Oxford Master Series in Condensed Matter Physics. Oxford University Press, 2009.

[6] J. Schwinger, “The theory of quantized fields. i,” *Phys. Rev.*, vol. 82, pp. 914–927, Jun 1951. [Online]. Available: https://link.aps.org/doi/10.1103/PhysRev.82.914

[7] J. H. Christenson, J. W. Cronin, V. L. Fitch, and R. Turlay, “Evidence for the 2π decay of the k_2^0 meson,” *Phys. Rev. Lett.*, vol. 13, pp. 138–140, Jul 1964. [Online]. Available: https://link.aps.org/doi/10.1103/PhysRevLett.13.138

[8] C. Abel *et al.*, “Measurement of the permanent electric dipole moment of the neutron,” *Phys. Rev. Lett.*, vol. 124, p. 081803, Feb 2020. [Online]. Available: https://link.aps.org/doi/10.1103/PhysRevLett.124.081803

[9] I. G. Irastorza, “An introduction to axions and their detection,” *SciPost Physics Lecture Notes*, mar 2022. [Online]. Available: https://doi.org/10.21468%2Fscipostphyslectnotes.45

[10] F. Wilczek, “Axions and the dark matter problem,” Theoretical Seminar, ITMO, April 2021. [Online]. Available: https://www.youtube.com/watch?v=3EjezghXkaw

[11] A. Abeln *et al.*, “Conceptual design of babyiaxo, the intermediate stage towards the international axion observatory,” 2021.

[12] I. P. Stern, ADMX, and A.-H. collaborations, “Axion dark matter searches,” in *AIP Conference Proceedings*. AIP Publishing LLC, 2014. [Online]. Available: http://dx.doi.org/10.1063/1.4883465

[13] T. Dafni and J. Galán, “Digging into axion physics with (baby)iaxo,” *Universe*, vol. 8, no. 1, 2022. [Online]. Available: https://www.mdpi.com/2218-1997/8/1/37

[14] I. G. Irastorza and J. Redondo, “New experimental approaches in the search for axion-like particles,” *Progress in Particle and Nuclear Physics*, vol. 102, pp. 89–159, 2018. [Online]. Available: https://www.sciencedirect.com/science/article/pii/S014664101830036X

[15] P. Sikivie, “Detection rates for “invisible”-axion searches,” *Phys. Rev. D*, vol. 32, pp. 2988–2991, Dec 1985. [Online]. Available: https://link.aps.org/doi/10.1103/PhysRevD.32.2988

[16] K.-S. Isleif, “The any light particle search experiment at desy,” *Moscow University Physics Bulletin*, vol. 77, no. 2, p. 120?125, Apr. 2022. [Online]. Available: http://dx.doi.org/10.3103/S002713492202045X

[17] E. Armengaud *et al.*, “Physics potential of the international axion observatory (iaxo),” *Journal of Cosmology and Astroparticle Physics*, vol. 2019, no. 06, p. 047, jun 2019. [Online]. Available: https://dx.doi.org/10.1088/1475-7516/2019/06/047

[18] C. G. A. Forstner, “Characterization of a TRISTAN Silicon Drift Detector Array with a Laser System,” Master’s thesis, Technical University of Munich, March 2023.

[19] “An Introduction to Silicon Drift Detectors,” Thermo Fisher Scientific - Materials & Structural Analysis, May 2015. [Online]. Available: https://www.azom.com/article.aspx?ArticleID=11973

[20] C. Bruch, “Characterisation of a 166-Pixel TRISTAN Detector Module in the KATRIN Monitor Spectrometer,” Master’s thesis, Technical University of Munich, March 2023.

[21] S. Mertens *et al.*, “A novel detector system for katrin to search for kev-scale sterile neutrinos,” *Journal of Physics G: Nuclear and Particle Physics*, vol. 46, no. 6, p. 065203, may 2019. [Online]. Available: https://dx.doi.org/10.1088/1361-6471/ab12fe

[22] J. P. Ulloa Beteta, “Characterization of a prototype silicon drift detector for the IAXO experiment,” Bachelor’s Thesis, Technical University of Munich, July 2022.

[23] D. Schlosser *et al.*, “Expanding the detection efficiency of silicon drift detectors,” *Nuclear Instruments and Methods in Physics Research Section A: Accelerators, Spectrometers, Detectors and Associated Equipment*, vol. 624, pp. 270–276, 12

2010.

[24] "Annual report 2017," Annual Report, Laboratorio Subterráneo de Canfranc, 2018. [Online]. Available: https://lsc-canfranc.es/wp-content/uploads/2019/03/2017_EN.pdf

[25] J. Pérez-Pérez *et al.*, "Radon mitigation applications at the laboratorio subterráneo de canfranc (lsc)," *Universe*, vol. 8, no. 2, 2022. [Online]. Available: https://www.mdpi.com/2218-1997/8/2/112

[26] A. Thompson *et al.*, "X-Ray Data Booklet. Center for X-ray Optics and Advanced Light Source," October 2009. [Online]. Available: https://xdb.lbl.gov/

[27] C. Wiesinger, personal communication.

[28] ——, "Background Index Simulation for the TAXO demonstrator with GEANT-4 ," personal communication.

[29] J. E. Eberhardt, "Fano factor in semiconductor radiation detectors," Master's thesis, School of Electrical Engineering and Telecommunications UNSW, Sydney, 1970. [Online]. Available: http://hdl.handle.net/1959.4/62470

[30] U. Fano, "Ionization yield of radiations. ii. the fluctuations of the number of ions," *Phys. Rev.*, vol. 72, pp. 26–29, Jul 1947. [Online]. Available: https://link.aps.org/doi/10.1103/PhysRev.72.26

[31] R. C. Alig, S. Bloom, and C. W. Struck, "Scattering by ionization and phonon emission in semiconductors," *Phys. Rev. B*, vol. 22, pp. 5565–5582, Dec 1980. [Online]. Available: https://link.aps.org/doi/10.1103/PhysRevB.22.5565

[32] G. J. Feldman and R. D. Cousins, "Unified approach to the classical statistical analysis of small signals," *Physical Review D*, vol. 57, no. 7, pp. 3873–3889, apr 1998. [Online]. Available: https://doi.org/10.1103%2Fphysrevd.57.3873

[33] S. Chu, L. Ekström, and R. Firestone. (1999, February). [Online]. Available: http://nucleardata.nuclear.lu.se/toi/index.asp

[34] M. Lépy, B. Duchemin, and J. Morel, "Comparison of experimental and theoretical l x — ray emission probabilities of 241am, 239pu and 240pu," *Nuclear Instruments and Methods in Physics Research Section A: Accelerators, Spectrometers, Detectors and Associated Equipment*, vol. 353, no. 1, pp. 10–15, 1994. [Online]. Available: https://www.sciencedirect.com/science/article/pii/0168900294915911

Abbreviations

ADC	analog-to-digital converter
ALPS	Any Light Particle Search
ALPs	axion-like-particles
ASIC	application-specific integrated circuit
CAST	CERN Axion Solar Telescope
CP	charge-parity
CPT	charge-parity-time
DAQ	data acquisition
DESY	Deutsches Elektronen-Synchrotron (en: German Electron Synchrotron)
GUI	graphical user interface
HERA	Hadron-Elektron-Ringanlage (en: Hadron-Electron Ring Accelerator)
IAXO	International Axion Observatory
KATRIN	Karlsruhe Tritium Neutrino Experiment
LSC	Laboratorio Subterráneo Canfranc
LSW	light shining through a wall
PCB	printed circuit board
PQ	Peccei-Quinn
QCD	quantum chromodynamics
SDD	silicon drift detector
SNR	signal-to-noise
TAXO	TRISTAN detector in IAXO
TRISTAN	Tritium Investigations on Sterile to Active Neutrino mixing

List of Figures

List of Tables

Acknowledgements

I would like to give my thanks to everybody who supported me during this thesis and my studies. I owe a lot to You and I am very grateful to have met people willing to share their knowledge with me, who took time to answer questions - especially since most times they had other things to do and I was not their responsibility, who helped me with my code, the hardware setup and who were not only of great help but a wonderful company, too. This blend made my days.

Prof. Dr. Susanne Mertens - Thank You for giving me the opportunity to first be a working student at Your group and to then continue as a master student with my thesis. I was able to work both on the hardware to gather data and the software side for the analysis of my collected data. Thanks to You I had the possibility to be a part of the IAXO collaboration and I was able to get an insight into a scientific community beyond my university. I am very grateful for Your support and all the helpful remarks regarding my thesis and my studies.

Dr. Christoph Wiesinger and Dr. Frank Edzards - Thank You for the great supervision, including all hints about hardware and coding help, for being great travel companions to the LSC lab and proof readers of this thesis. As well as answering questions, sometimes more than once and pointing me in the right direction on what to do next.

IAXO collaboration & LSC staff and especially Alfonso and Juan for restarting our setup, babysitting it and giving us a warm welcome in Canfranc and Jaca.

TAXO team - I am very glad to have had more than cooperative team members. Whenever I needed code, a technical drawing or somebody to look over my analysis, soldering work or ideas, I was always able to find an answer to my questions.

Daniel - You were the first face of E47 I met, I got a great lab tour and You made me feel welcome. You gave me all the contacts I needed at the MPP as well as in the group. Without this starting help many small tasks would have been a lot harder to complete. I am very grateful for all the continued hands-on comments, many of which made working in the laboratory significantly easier.

Korbinian - Your insight into all lab and hardware related topics is priceless. Thank You for taking the time to explain. Especially when I came back to ask the same question again.

Matthias - Thank You for easily lending me soldering equipment I urgently needed and all the interesting conversations.
E47 members - for great lunch, coffee & ice cream breaks, cake seminars and after work activities (both the sports and relaxed group evenings). Such a friendly and supportive working atmosphere is the best I could have hoped for.
Dr. M. Saß, Dr. B. Schaper, K. Bannert - Thank You for supporting me through my studies with organisational help while being uncomplicated and easy to reach.
MPP and TUM workshops - Thank You for accepting technical drawings, manufacturing exactly what was needed, modifying items to perfection and allowing me to work at the soldering bench (MPP).
Terry Weinmann - Thank You for skimming over several shopping-wish-lists. Else I would probably still wait for some cables while being stuck with hundreds of contact adapters I did not actually want.
uncounted wikipedia authors - Thank You for expanding my horizons in various directions and providing a starting point when looking for explanations and deep dives into foreign topics. I cannot imagine studying without this amazing tool You have created.
Coraly, Lena, Constanze, Hanya, Gerhard, Weronika, Jacky, Patrick, Magdalena, Konstantin, Stefan, Thomas, Sofia, Florence, Benedicte, Camilla, Ranjith, Motaz, Steffen, Anna, the 7-7 group, IsoKor and Delta - Thank You for great evenings, coffee breaks and endless conversations be it in person or remotely.
Christoph K. - for support, endurance and two pairs of ears.
Family - for enduring my extended study journey and unwavering support.
Jan&Dominik - the best brothers I could wish for. Nie do zapomnienia pózne rozmowy wieczorne jak i dyskusje. Z wami to jest o wiele weselej i ciekawiej, nie zależnie czy to filmy z własnym komentarzem i dubbingiem czy techniczne rozmowy o samolotach i zaletach maszyn kuchennych z ich kosztorysem.
Parents - Dziękuje. Wiem jaki mam przywilej mając takich rodziców i taką rodzine. Za rzadko za nią dziękuję.

A Current axion constraints

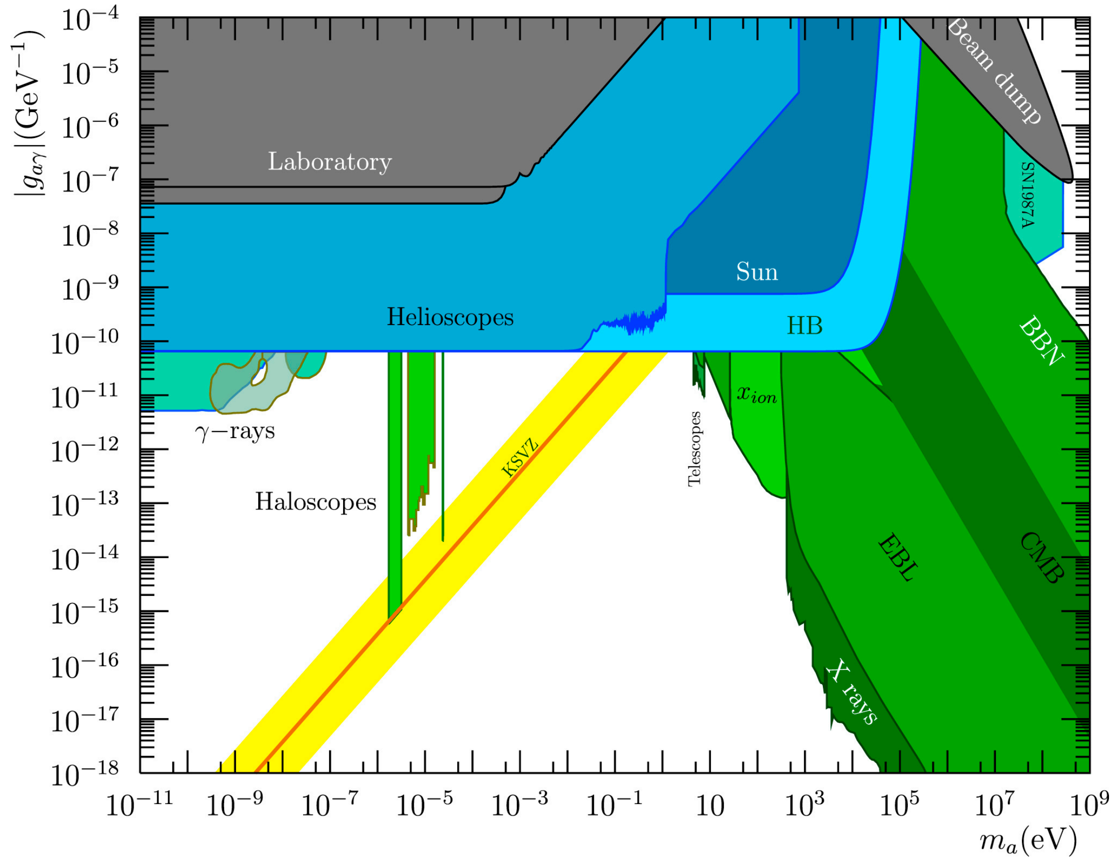

Figure A.1: Current axion constraints without upcoming experiments. In green cosmological constraints including haloscope results are given. Helioscope results as well as bounds obtained from stars are blue. Grey areas are bounds provided by LSW experiments. The QCD-axion hinted region is the yellow band. Explanation and figure taken from [14].

B Runlist and settings of devices and software

B.1 Runlist

	Board B		Board A		
runs	run001	run002	-	run003	run004 - run022
function	calibration with ^{241}Am	overnight measurement	test for noise - passed	calibration with ^{241}Am	background measurement
comments	channel 5 had random telegraph noise	too much noise during calibration; conclusion to switch to board A	less noise than for board B	successful calibration	successful datataking

Table B.1: Overview over the content of the runs. Board B was exchanged due to too high noise levels. Board A had a better performance, resulting in successful data taking.

B.2 Settings

B.2.1 Bias system

The power supply (appendix B.2.2) provides the bias system with the correct voltage. The bias system by `XG-Lab` in turn provides the correct voltages for the detector. The low and high voltages can be found in tables B.2 and B.3 respectively.

name	V
rel_L	-9.98
res_H	4.0
-5V	-5
5V	-4.98
V_curr	2.86
V_ref	2.86
V_sss	-1.1
V_d	6.17

Table B.2: Low voltages of the bias board.

name	V
R1	-8.95
RX	-120
IGR	-18.9
BC	-100.2
BF	-110.1

Table B.3: High voltages of the bias board.

name	V
BW	1.1
VTH	2.5
VCURR	2.7
VREF	2.7
Offset	0

Table B.4: Voltages set in the graphical user interface (GUI) of the bias board.

boards on	3
channels on	1-7
detector High Voltage	ON
detector Low Voltage	ON
Low Gain Mode	OFF
Select Pre	OFF
available modules	SN 2573
varying values	
V_SSS	1.076 mA
V_d current	1.801 mA
Temperature	1.707 V

Table B.5: Bias board - other settings.

B.2.2 Keithley power supply

The Keithley power supply of the 2230 series (`2230-30-1`) is powering the bias board. The voltage was set to 24 V and the current automatically sets itself.

B.2.3 CAEN Digital Detector Emulator

The pulser is the `CAEN DT5810B Fast Digital Detector Emulator`. It was set to the lowest possible frequency (0.5 Hz). The pulser can be controlled through a desktop app, which provides a inspection mode. This mode shows the runtime of the pulser as well as the number of signals sent out by the pulser. As the pulser mode was set to a Poissonian distribution, the distance between pulses is changing. With the inspection mode a rate was calculated of 0.46 Hz, which was lower than the set frequency. The calculated frequency was used for the background determination. The reason for the discrepancy between set frequency and calculated one was not further investigated.

Energy	fixed
LSB	1267*
V	0.3
Time base	Poisson
kHz	0.0005
Shape	
Rise (µs)	0.2
Tau (µs)	100

Table B.6: Settings of the pulser GUI.
*automatic, depends on V

B.2.4 CoMPASS settings

In order to enable the global trigger, a file has to be loaded. It can be obtained from CAEN.

mode	wave
timed run (in seconds)	no
save RAW data	yes
file format	bin
limited file size	100 MB
file saving option - single/oneFilePerChannel	OneFilePerChannel
file saving option - if single selected - time sorting (yes/no)	Not applicable
energy format	ADC channel
spectra saving	Yes
format	.txt
type	Energy

Table B.7: CoMPASS acquisition settings.

Name	V1782_38
ADC bits	16
ROC firmware	4.25 build 5510
Link	A4818 PID 22837, chain node #0
ID	0-16-38
Sampling rate (MS/s)	100.00
AMC firmware	128.78 build 6825
Status	connected
Model	V1782
DPP type	DPP_PHA
License	Licensed
Enable	ON

Table B.8: CoMPASS - board settings.

Enable	yes
Record length	40000
Trace length	-
Pre-trigger	20000
Polarity	negative
N samples baseline	1024
DC Offset	channel 0-6: 65%; channel 7: 15%
Course gain	1

Table B.9: CoMPASS - board settings - input.

Threshold	run003: 150lsb - for all channels; run004 & run005: 180lsb; run006 - run010, run012 - run022: 220lsb for channel 01, 180lsb all other channels; run011: 220lsb for all channels
Trigger holdoff	400ns
Fast Disc. smoothing	32
Input risetime	800ns

Table B.10: CoMPASS - board settings - discriminator.

Trap. rise time	4.0 µs
Trap. flat top	0.3 µs
Trap. pole zero	channel 0-6: 14 µs; channel 7: 100 µs
Peaking time	50 %
N samples peak	1
Peak holdoff	0.960 µs
Energy fine gain	1

Table B.11: CoMPASS - board settings - trapezoid.

type	Custom
Addess 0x	0
Ch	0
Value 0x	0 0000

Table B.12: CoMPASS - board settings - registers.

Energy N channels	32768
PSD N channels	16384
Time intervals N channels	8192
Time intervals Tmin	0.000 µs
Time intervals Tmax	1000.000 µs
Start/stop dt N channels	8192
start/stop dt Tmin	−1000 ns
start/stop dt Tmax	1000 ns
2D Energy N channels	128
2D PSD N channels	128
2D dt N channels	128

Table B.13: CoMPASS - board settings - spectra.

Saturation rejection	off
Pileup rejection	off
E low cut	0
E high cut	0
E cut enable	off
PSD low cut	0
PSD high cut	0
PSD cut enable	off
Time intervals low cut	0 ns
Time intervals high cut	0 ns
Time intervals cut enable	off

Table B.14: CoMPASS - board settings - rejections.

C0	0
C1	1.000
C2	0
Calibration units	keV

Table B.15: CoMPASS - board settings - energy calibration.

Start mode	Software (asynchronous)
TRG OUT /GPO mode	Global ch. OR
Start delay	0 ns
Channel time offset	0.000 ns

Table B.16: CoMPASS - board settings - synchronisation.

Coincidence Mode	DISABLED*
Coincidence Window	100 ns

Table B.17: CoMPASS - board settings - trigger/veto/coincidences.
*from run011 onwards, before it could have been ON

Label	CH
FPIO type	NIM*
Rate optimisation	32

Table B.18: CoMPASS - board settings - miscellaneous.
*from run011 onwards, before it could have been TTL

Correlation	Disabled
Reference Channel	not applicable
Reference board	not applicable
Correlation window (µs)	not applicable

Table B.19: CoMPASS - board settings - time selection.

Event building mode	Disabled

Table B.20: CoMPASS - board settings - virtual channels.

C Americium Lines[2]

Number	Element	Line	Energy (keV)	Relative intensity	Source
1a	$_{22}$Ti	$K_{\alpha 2}$	4.505	6.4	[26]
1b	$_{22}$Ti	$K_{\alpha 1}$	4.511	12.8	[26]
2	$_{56}$Ba	$L_{\beta 1}$	4.828	2.47	[26]
3a	$_{26}$Fe	$K_{\alpha 2}$	6.391	10.2	[26]
3b	$_{26}$Fe	$K_{\alpha 1}$	6.404	20.2	[26]
4	$_{26}$Fe	$K_{\beta 1,3}$	7.058	3.63	[26]
5a	$_{28}$Ni	$K_{\alpha 2}$	7.461	12.2	[26]
5b	$_{28}$Ni	$K_{\alpha 1}$	7.478	24.0	[26]
6a	$_{29}$Cu	$K_{\alpha 2}$	8.028	13.3	[26]
6b	$_{29}$Cu	$K_{\alpha 1}$	8.048	26.0	[26]
7a	$_{28}$Ni	$K_{\beta 1,3}$	8.265	4.36	[26]
7b	$_{78}$Pt	L_{l}	8.266	0.58	[26]
8a	$_{30}$Zn	$K_{\alpha 2}$	8.616	14.3	[26]
8b	$_{30}$Zn	$K_{\alpha 1}$	8.639	28.0	[26]
9	$_{29}$Cu	$K_{\beta 1,3}$	8.905	4.69	[26]
10a	$_{78}$Pt	$L_{\alpha 2}$	9.362	1.26	[26]
10b	$_{78}$Pt	$L_{\alpha 1}$	9.443	11.2	[26]
11	$_{78}$Pt	L_{η}	9.975	0.163	[26]
12a	$_{78}$Pt	$L_{\beta 6}$	10.840	0.160	[26]
12b	$_{78}$Pt	$L_{\beta 4}$	10.854	0.083	[26]
12c	$_{78}$Pt	$L_{\beta 1}$	11.071	7.5	[26]
12d	$_{78}$Pt	$L_{\beta 3}$	11.235	0.109	[26]
12e	$_{78}$Pt	$L_{\beta 2,15}$	11.242	2.69	[26]
12f/13a	$_{78}$Pt	$L_{\beta 5}$	11.562	0.222	[26]
13b	$^{237}_{93}$Np	L_{l}	11.871	0.00864	[33] [34]
14	$_{78}$Pt	$L_{\gamma 1}$	12.942	1.47	[26]
15a	$_{78}$Pt	$L_{\gamma 2}$	13.273	0.027	[26]
15b	$_{78}$Pt	$L_{\gamma 3}$	13.361	0.037	[26]
16a	$^{237}_{93}$Np	$L_{\alpha 2}$	13.761	0.0115	[33] [34]
16b	$^{237}_{93}$Np	$L_{\alpha 1}$	13.946	0.1188	[33] [34]
17	Unknown (1)				
18	$^{237}_{93}$Np	L_{η}	15.861	0.00369	[33] [34]
19	$^{237}_{93}$Np	$L_{\beta 6}$	16.109	0.00246	[33] [34]
20a	$^{237}_{93}$Np	$L_{\beta 15}$	16.79	0.0012	[34]

20b	$^{237}_{93}$Np	$L_{\beta 2}$	16.816	0.0259	[33] [34]
20c	$^{237}_{93}$Np	$L_{\beta 4}$	17.061	0.0176	[33] [34]
20d	$^{237}_{93}$Np	$L_{\beta 7}$	17.27	0.0020	[34]
21a	$^{237}_{93}$Np	$L_{\beta 5}$	17.505	0.00465	[33] [34]
21b	$^{237}_{93}$Np	$L_{\beta 1}$	17.751	0.1160	[33] [34]
21c	$^{237}_{93}$Np	$L_{\beta 3}$	17.992	0.01222	[33] [34]
22a	$^{237}_{93}$Np	$L_{\beta 10}$	18.58	0.00075	[34]
22b	$^{237}_{93}$Np	$L_{\beta 9}$	18.76	0.00108	[34]
23	$^{237}_{93}$Np	$L_{\gamma 5}$	20.10	0.00121	[33] [34]
24a	$^{237}_{93}$Np	$L_{\gamma 1}$	20.784	1.39	[33]
24b	$^{237}_{93}$Np	$L_{\gamma 2}$	21.099	0.65	[33]
25a	$^{237}_{93}$Np	$L_{\gamma 8}$	21.26	0.00452	[34]
25b	$^{237}_{93}$Np	$L_{\gamma 3}$	21.342	0.0047	[33] [34]
25c	$^{237}_{93}$Np	$L_{\gamma 6}$	21.491	0.0060	[33] [34]
26a	$^{237}_{93}$Np	$L_{\gamma 4}$	22.22	0.00197	[34]
26b	$^{237}_{93}$Np	$L_{\gamma 13}$	22.38	0.00058	[34]
27a	$_{50}$Sn	$K_{\alpha 2}$	25.044	24.7	[26]
27b	$_{50}$Sn	$K_{\alpha 1}$	25.271	45.7	[26]
28	$^{237}_{93}$Np	Gamma (1)	26.345	2.40	[33]
29a	$_{50}$Sn	$K_{\beta 3}$	28.444	4.15	[26]
29b	$_{50}$Sn	$K_{\beta 1}$	28.486	7.99	[26]
30	$_{56}$Ba	$K_{\alpha 2}$	31.817	25.6	[26]
31a	$^{237}_{93}$Np	Gamma (2)	32.183	0.0174	[33]
31b	$_{56}$Ba	$K_{\alpha 1}$	32.194	46.7	[26]
32	$^{237}_{93}$Np	Gamma (3)	33.196	0.126	[33]
33	Unknown (2)				
34a	$_{56}$Ba	$K_{\beta 3}$	36.304	4.47	[26]
34b	$_{56}$Ba	$K_{\beta 1}$	36.378	8.63	[26]
35	$_{56}$Ba	$K_{\beta 2}$	37.255	2.73	[26]
36	$^{237}_{93}$Np	Gamma (4)	43.423	0.073	[33]
33	Unknown (3)				
37b	$^{237}_{93}$Np	Gamma (5)	59.541	35.9	[33]

Table C.1: Nomenclature of all relevant photons with their energies and relative intensities - taken from [2].

feature name	peak type	peak number	energy in (keV)	category	description	usable
B	X-ray	10b	9.443	4	distinct single X-ray peak in noise	yes
C	X-ray	12e	11.400	6	overlapping X-ray peak (≈100 counts)	yes
D	X-ray	16b	13.964	6	overlapping but distinct X-ray peak (>100 counts)	yes
F	X-ray	20b	16.816	6	overlapping X-ray peak (≈100 counts)	yes
G	X-ray	21b	17.751	6	overlapping but distinct X-ray peak (>100 counts)	yes
J	X-ray	24a	20.784	6	overlapping X-ray peak (≈100 counts)	yes
L	X-ray	26a	22.220	7	overlapping X-ray peak (≈100 counts)	yes
M	pulser	-	-	-	pulser peak	no
N	X-ray	27b	25.271	7	overlapping X-ray peak in noise	yes
O	gamma	28	26.345	1	distinct single photon peak close to a noise edge	yes
P	gamma	32	33.196	1	single photon peak vanishing in noise	no
Q	gamma	37b	59.541	1	distinct single photon peak in low noise	yes

Table C.2: Overview of the selected features of the measured ^{241}Am spectrum with energy, peak number (see number in table C.1) and category number (adapted from [2]). A good candidate for calibration has a low category number. With increasing category value the mean of the Gaussian fit will describe less precisely the actual position of the peak. All but two features can be used in this energy calibration.

Spectral peak B and spectral peak N were not included in the fit points. Spectral peak B could have been included, however, it was excluded due to faulty reasoning, which argued that spectral peaks below 10 keV were displayed distorted. This is not the case for photons, but true for electrons of energies below 10 keV. They experience a significant energy loss in the dead layer, which is a layer in the SDD where energy readout is only partially possible. Energy deposited there is therefore only partially recorded. These electron peaks are assigned a reduced energy value, which shows itself in a leftshift of the peak towards lower energies [20]. In [20] the impact of the dead layer can be seen for electrons.
Spectral peak N was absorbed by the more intense pulser peak in some channels. As the linear fit curves were supposed to be comparable, this overlap disqualified spectral peak N.

D Calibration data

channel	slope in (keV/ADC)	offset in (keV)	slope error	offset error
00	0.009384	-0.155674	0.000015	-0.043734
01	0.009197	-0.197391	0.000015	-0.045651
02	0.009510	-0.161182	0.000015	-0.044241
03	0.009549	-0.141688	0.000015	-0.043607
04	0.009628	-0.166965	0.000015	-0.043624
05	0.009546	-0.147185	0.000016	-0.045251
06	0.009571	-0.160796	0.000015	-0.042416

Table D.1: Linear fit parameters for the calibration function with errors. The arbitrary ADC value is multiplied with the slope value and the offset is added. The result is the energy in (keV).

D.1 Linear calibration fits for the other channels

Linear calibration curves with more details using the measured ^{241}Am spectrum are given in figs. D.1 to D.7. Figure D.3 displays the fit of a linear function in detail for channel 02. The first subplot shows the calibration function in green, where fitpoints are displayed as a red x and other peaks not included in the fit as blue x. The orange error bars are enlarged. The goodness of the linear fit can be seen in the three following subplots. The second subplot shows the deviation from the linear fit function as a value of sigma, while the third subplot shows the sigma in eV. The bottommost subplot has the deviation from the fit in percent. As all fitpoints have a deviation of less than one percent from the linear fit function, the fit function qualifies as a good one. The set of fitpoints is the same for all channels. These linear fits all contain the error with not including feature B, and assigning an incorrect energy of 11.400 keV instead of 11.242 keV to feature C.

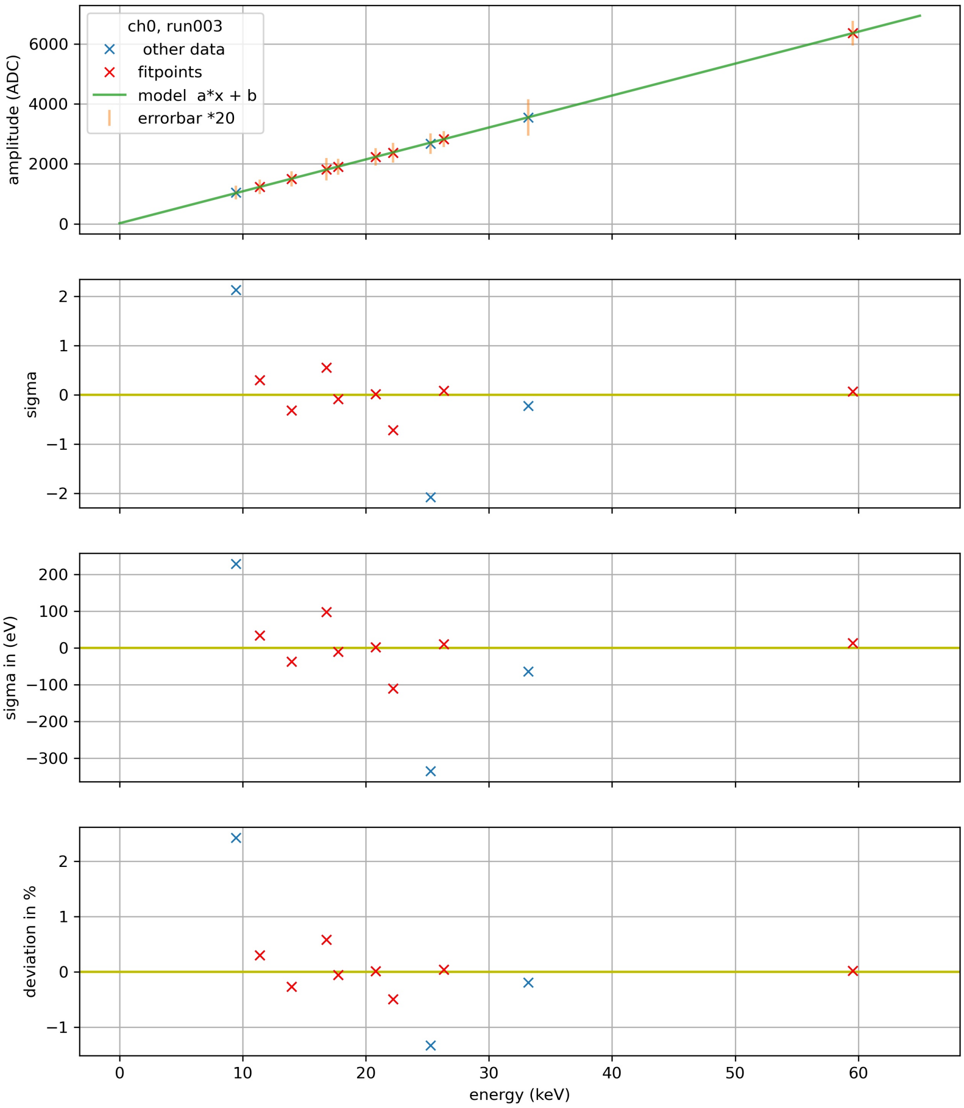

Figure D.1: Linear calibration function for channel 00. $a = 106.6$; $b = 16.6$

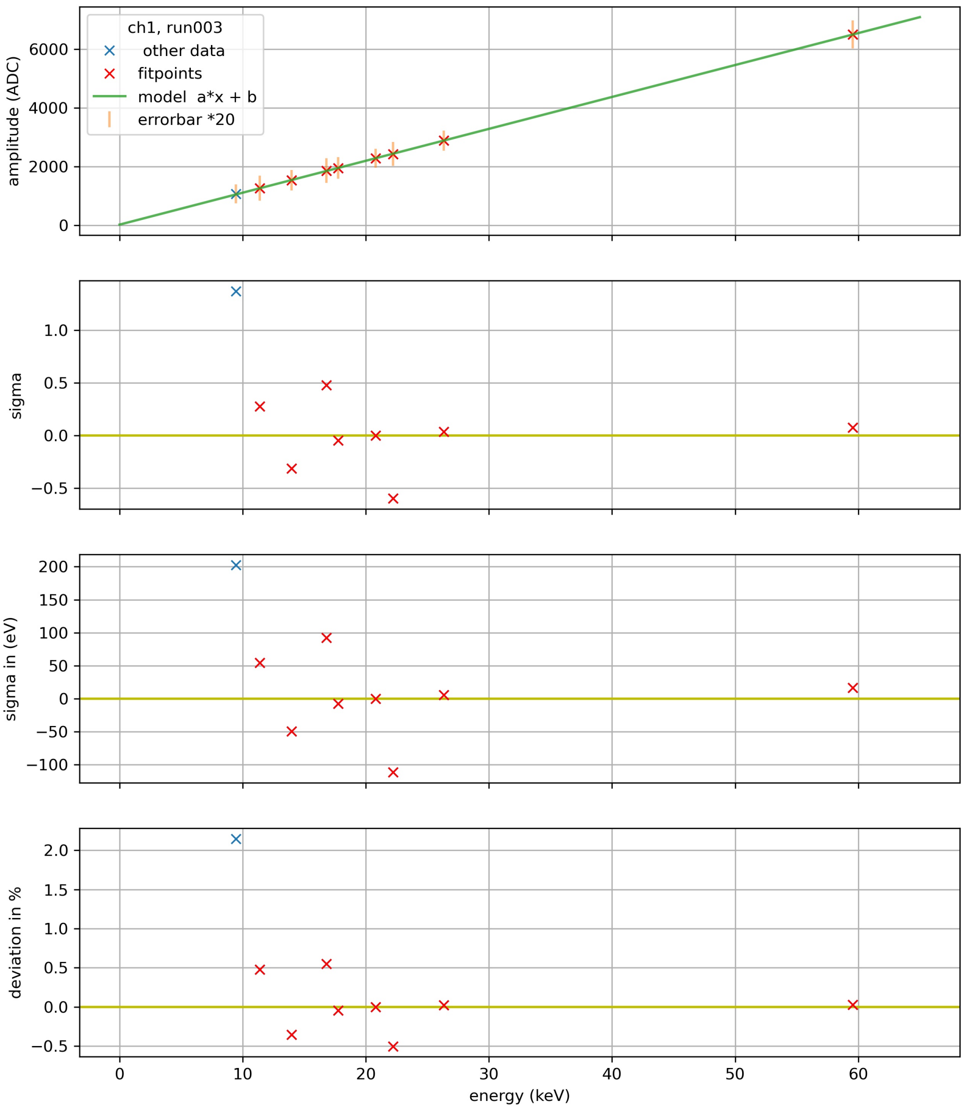

Figure D.2: Linear calibration function for channel 01. $a = 108.7$; $b = 21.5$

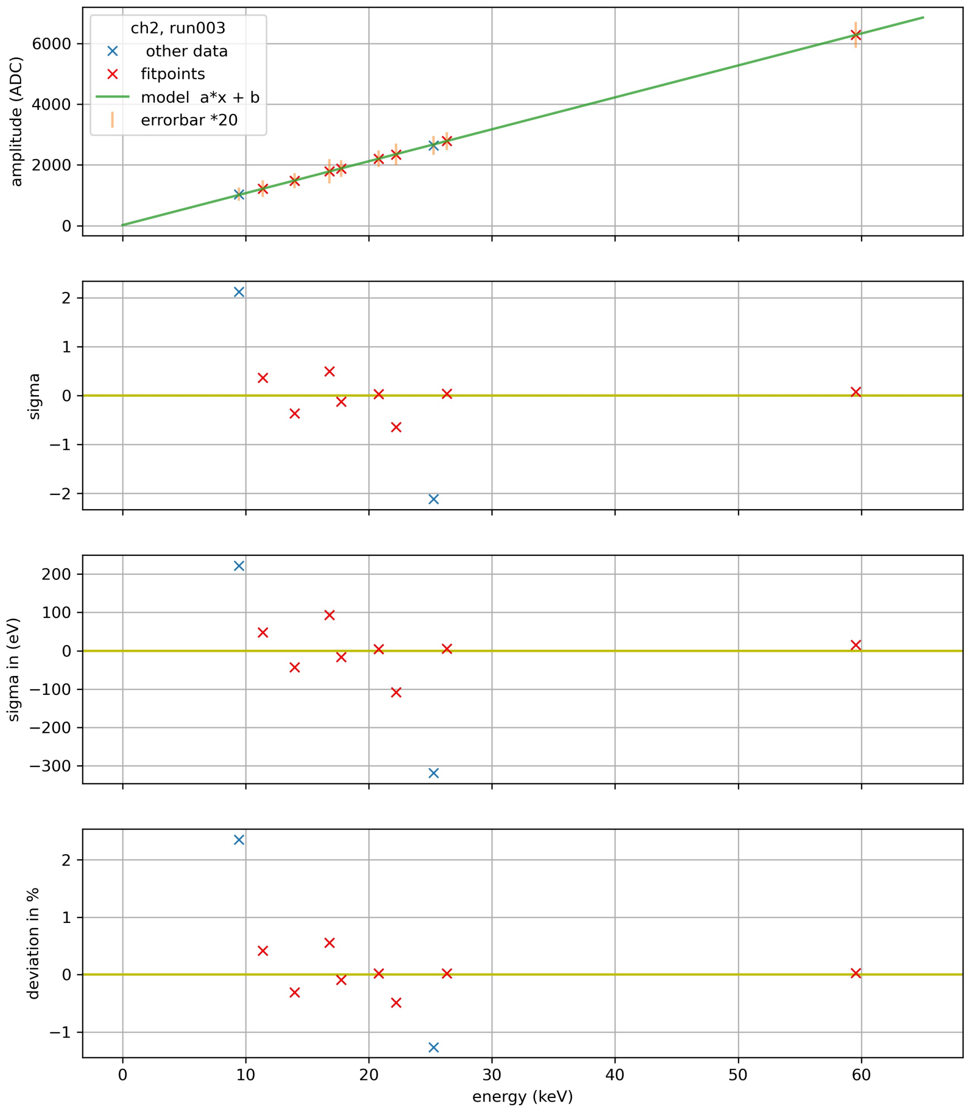

Figure D.3: Linear calibration function for channel 02. $a = 105.1$; $b = 16.9$

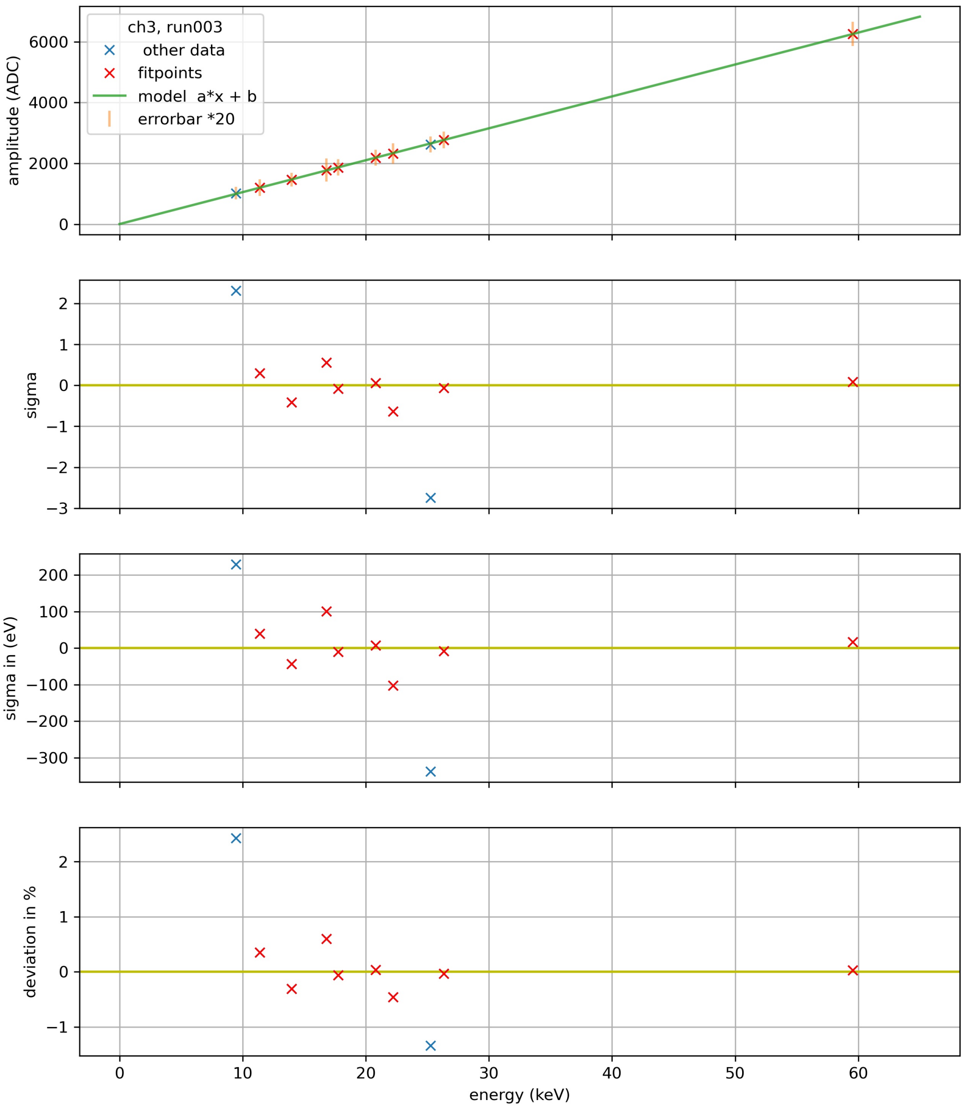

Figure D.4: Linear calibration function for channel 03. $a = 104.7$; $b = 14.8$

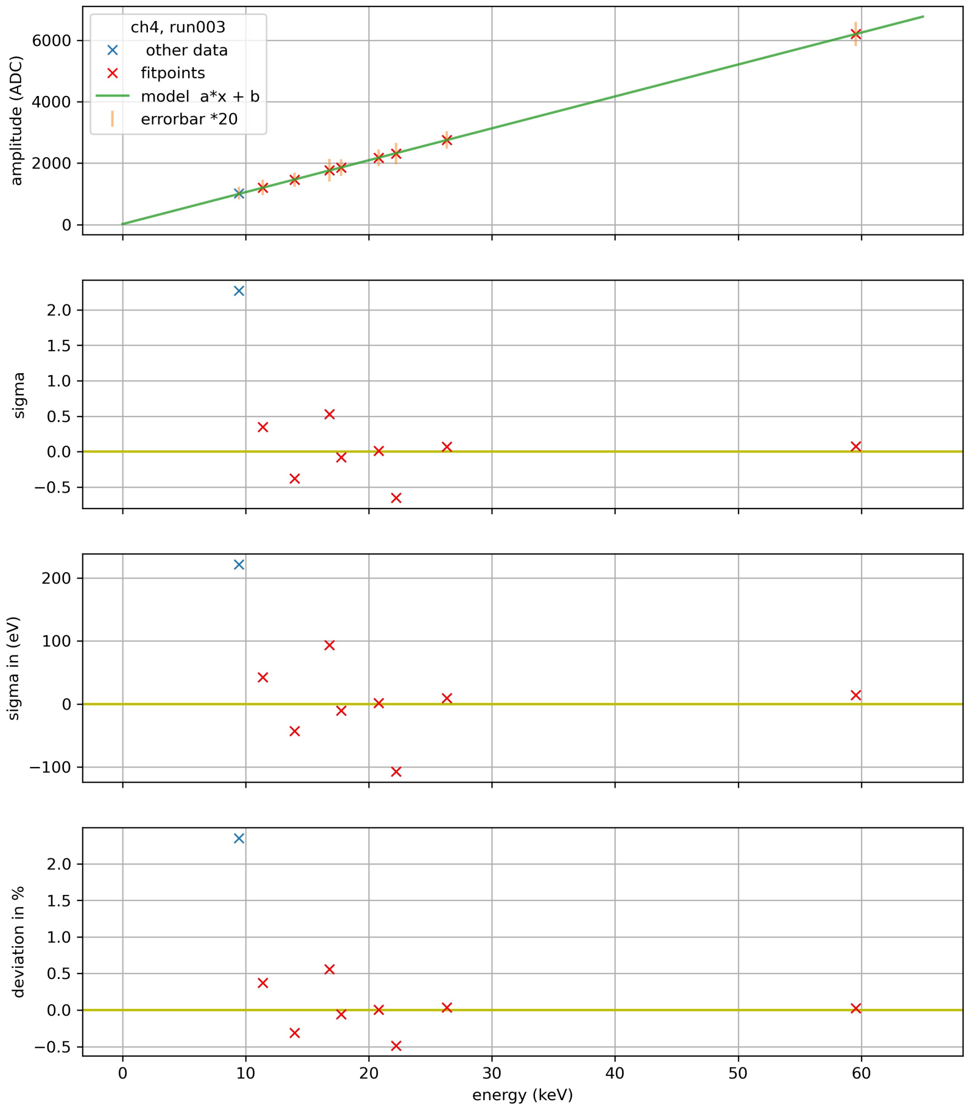

Figure D.5: Linear calibration function for channel 04. $a = 103.9$; $b = 17.3$

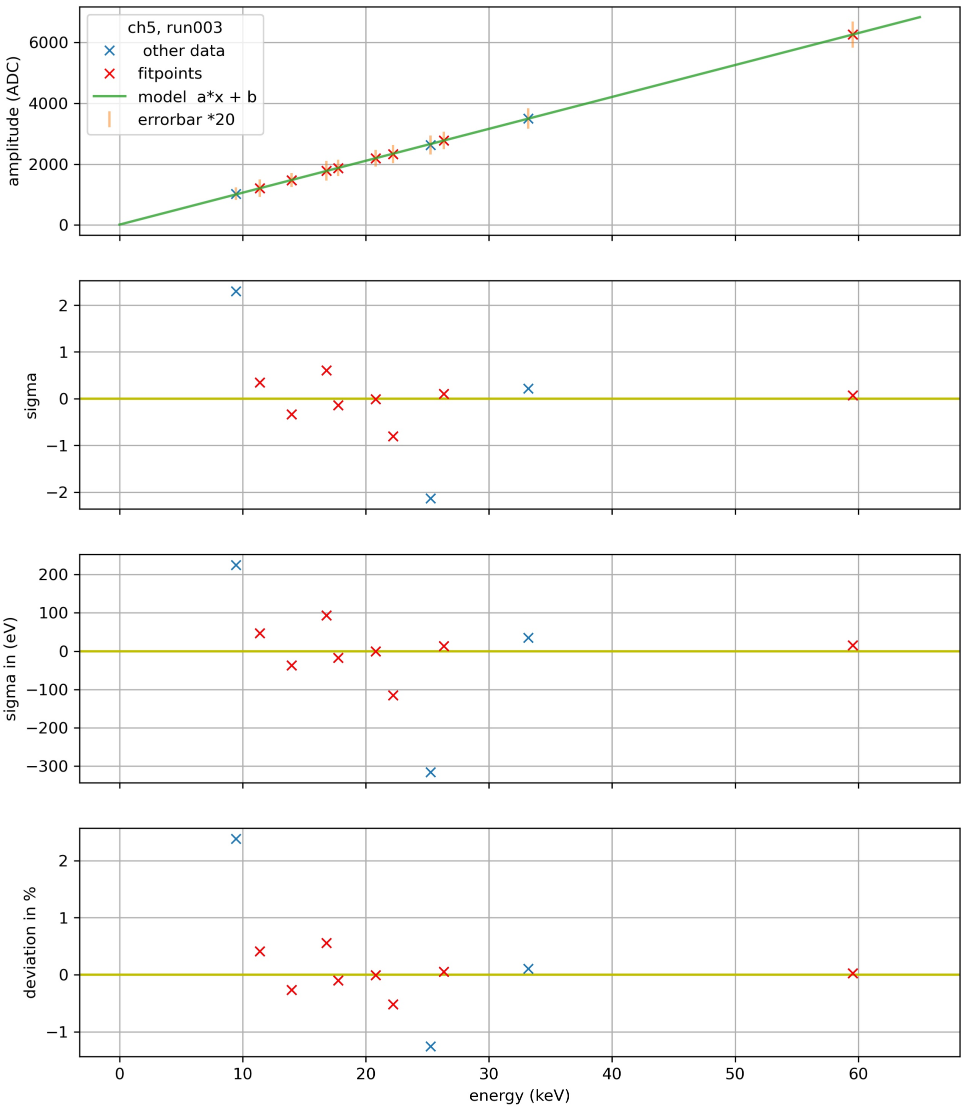

Figure D.6: Linear calibration function for channel 05. $a = 104.8$; $b = 15.4$

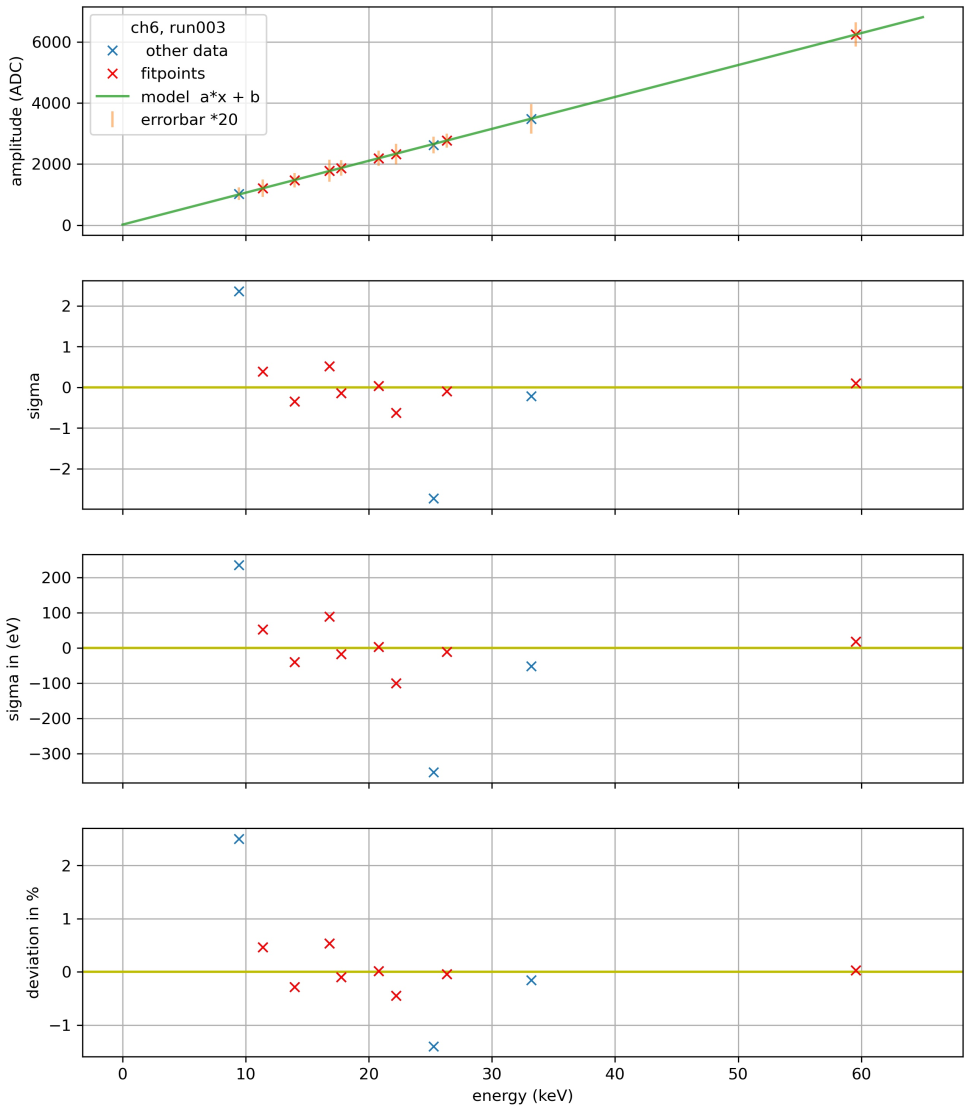

Figure D.7: Linear calibration function for channel 06. $a = 104.5$; $b = 16.8$

D.2 Corrected linear calibration fit

Figure D.8 contains the linear fit including feature *B* and with correct energy values for feature *C*. The new energy is given in table D.2. The difference is highlighted in green.

feature name	peak number	energy in (keV)	category	usable
B	10b	9.443	4	yes
C	12c	11.242	6	yes
D	16b	13.964	6	yes
F	20b	16.816	6	yes
G	21b	17.751	6	yes
J	24a	20.784	6	yes
L	26a	22.220	7	yes
M	-	-	-	no, pulser peak
N	27b	25.271	7	yes
O	28	26.345	1	yes
P	32	33.196	1	no, too few counts
Q	37b	59.541	1	yes

Table D.2: Corrected overview of the selected features of the measured ^{241}Am spectrum with energy, peak number (see number in table C.1) and category number (adapted from [2]). A good candidate for calibration has a low category number. With increasing category value the mean of the Gaussian fit will describe less precisely the actual position of the peak. All but two features can be used in this energy calibration. A more detailed description of the features is given in table C.2.

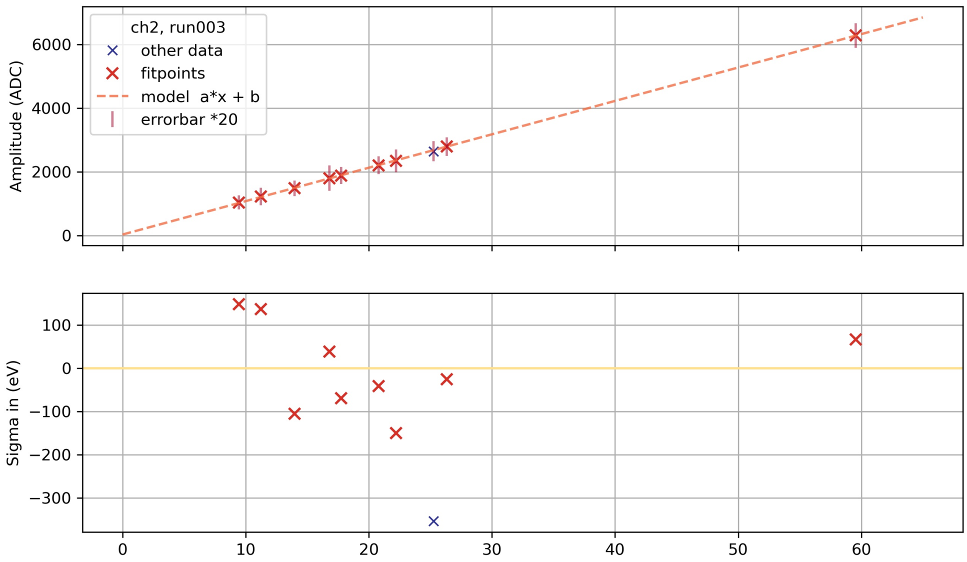

Figure D.8: Corrected linear calibration function, including feature B and the correct energy for feature C, for channel 02 with the ^{241}Am calibration data (top figure). The datapoints fit well to the assumed linear relation. The deviation of the fitpoints is randomly distributed and below 150 eV (bottom figure). The rejected feature N is displayed as well.

E Energy resolution

channel	0.0 keV	6.0 keV	10.0 keV	59.5 keV
00	228.49	256.87	274.16	434.51
01	365.42	383.80	395.58	519.73
02	223.87	252.77	270.32	432.10
03	256.79	282.34	298.16	450.04
04	251.73	277.74	293.81	447.17
05	242.24	269.17	285.72	441.90
06	208.83	239.55	258.01	424.51
Fano limit	0.0	117.36	151.52	369.59

Table E.1: Energy resolution in eV for selected energies for each channel determined from the energy resolution curves in fig. 4.6. Except for values for 59.5 keV, which were calculated by fitting a gaussian to spectral peak Q.

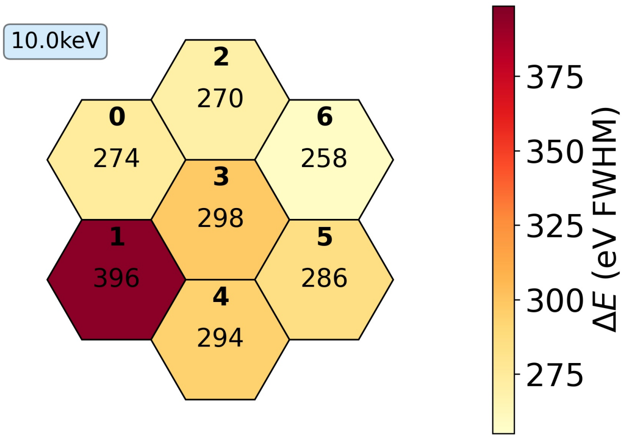

Figure E.1: Energy resolution for 10.0 keV in eV extrapolated from the Fano-curve based on the energy resolution of 59.5 keV. Pixel 1 shows a worse resolution than the other pixels.

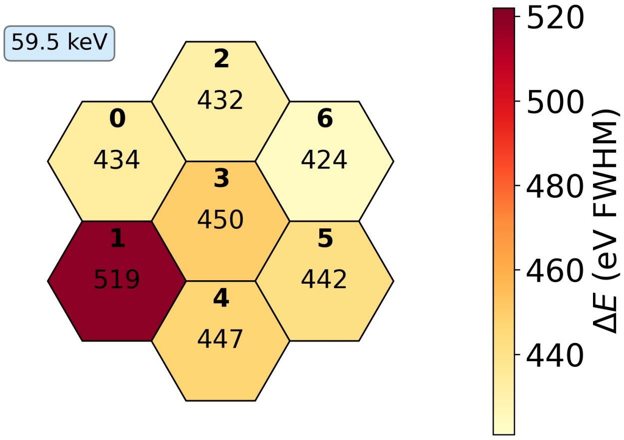

Figure E.2: Energy resolution for the 59.5 keV photon peak (Q peak) in eV, where pixel 1 shows a worse resolution than the other pixels.

F Data cleaning

channel	drift in keV	drift in %
00	-0.4147	1.494
01	-0.1202	0.486
02	-0.1432	0.601
03	-0.3116	1.310
04	-0.0466	0.188
05	-0.2399	1.018
06	-0.0879	0.360
Pulser	-	0.012

Table F.1: Drift values of the pulser for all channels including the pulser channel.

run	compl / total
3	1.000
4	0.927
5	0.999
6	1.000
7	1.000
8	1.000
9	1.000
10	1.000
11	0.998
12	0.929
13	0.901
14	0.905
15	0.908
16	0.952
17	0.904
18	0.984
19	0.554
20	0.980
21	0.958
22	0.999

Table F.2: Fraction of usable timestamps over the total number of recorded timestamps for each run.

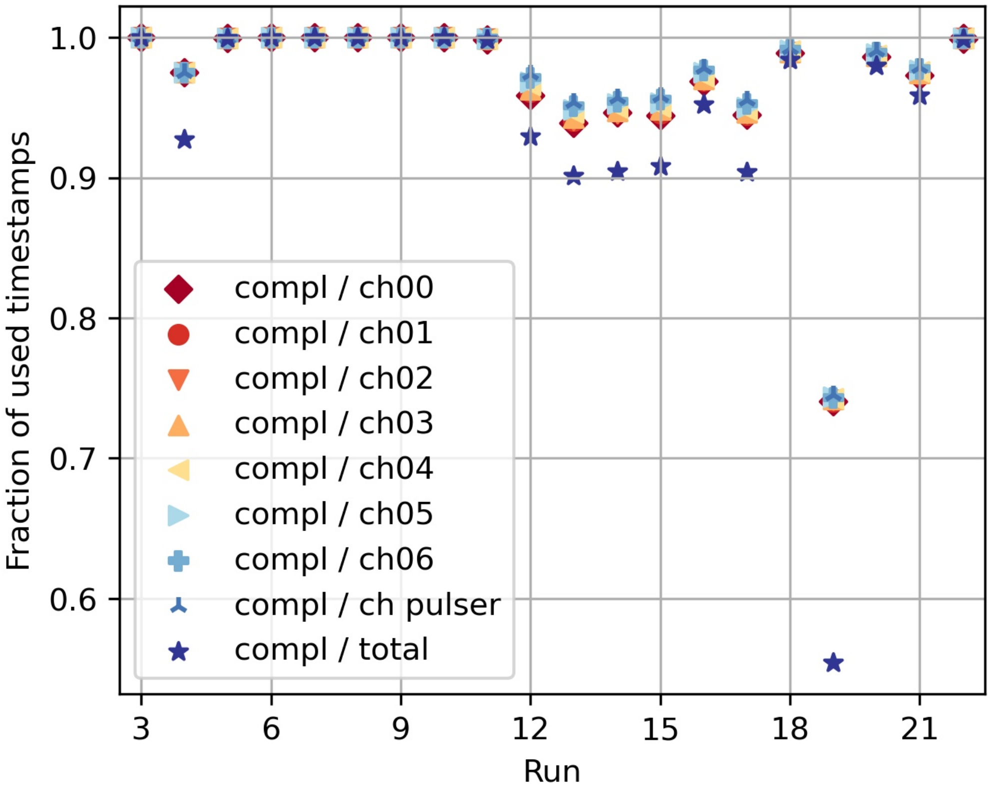

Figure F.1: Fraction of usable data due to time mismatch. *compl* - number of complete events in a run; *chxx* - number of recorded timestamps in channel xx; *total* - total number of timestamps for all channels of one run.